

Diagnosing spatial biases and uncertainties in global fire emissions inventories: Indonesia as regional case study



Tianjia Liu^{a,*}, Loretta J. Mickley^b, Miriam E. Marlier^c, Ruth S. DeFries^d, Md Firoz Khan^e, Mohd Talib Latif^f, Alexandra Karambelas^g

^a Department of Earth and Planetary Sciences, Harvard University, Cambridge, MA, USA

^b School of Engineering and Applied Sciences, Harvard University, Cambridge, MA, USA

^c RAND Corporation, Santa Monica, CA, USA

^d Department of Ecology, Evolution, and Environmental Biology, Columbia University, New York, NY, USA

^e Department of Chemistry, Faculty of Science, University of Malaya, Kuala Lumpur, Malaysia

^f School of Environmental and Natural Resource Sciences, Faculty of Science and Technology, Universiti Kebangsaan Malaysia, Bangi, Selangor, Malaysia

^g The Earth Institute, Columbia University, New York, NY, USA

ARTICLE INFO

Keywords:

Fire emissions
MODIS
Burned area
Active fires
Smoke
Indonesia
Google Earth Engine

ABSTRACT

Models of atmospheric composition rely on fire emissions inventories to reconstruct and project impacts of biomass burning on air quality, public health, climate, ecosystem dynamics, and land-atmosphere exchanges. Many such global inventories use satellite measurements of active fires and/or burned area from the Moderate Resolution Imaging Spectroradiometer (MODIS). However, differences across inventories in the interpretation of satellite imagery, the emissions factors assumed for different components of smoke, and the adjustments made for small and obscured fires can result in large regional differences in fire emissions estimates across inventories. Using Google Earth Engine, we leverage 15 years (2003–2017) of MODIS observations and 6 years (2012–2017) of observations from the higher spatial resolution Visible Imaging Infrared Radiometer Suite (VIIRS) sensor to develop metrics to quantify five major sources of spatial bias or uncertainty in the inventories: (1) primary reliance on active fires versus burned area, (2) cloud/haze burden on the ability of satellites to “see” fires, (3) fragmentation of burned area, (4) roughness in topography, and (5) small fires, which are challenging to detect. Based on all these uncertainties, we devise comprehensive “relative fire confidence scores,” mapped globally at $0.25^\circ \times 0.25^\circ$ spatial resolution over 2003–2017.

We then focus on fire activity in Indonesia as a case study to analyze how the choice of a fire emissions inventory affects model estimates of smoke-induced health impacts across Equatorial Asia. We use the adjoint of the GEOS-Chem chemical transport model and apply emissions of particulate organic carbon and black carbon (OC + BC smoke) from five global inventories: Global Fire Emissions Database (GFEDv4s), Fire Inventory from NCAR (FINNv1.5), Global Fire Assimilation System (GFASv1.2), Quick Fire Emissions Dataset (QFEDv2.5r1), and Fire Energetics and Emissions Research (FEERv1.0-G1.2). We find that modeled monthly smoke $PM_{2.5}$ in Singapore from 2003 to 2016 correlates with observed smoke $PM_{2.5}$, with r ranging from 0.64–0.84 depending on the inventory. However, during the burning season (July to October) of high fire intensity years (e.g., 2006 and 2015), the magnitude of mean Jul-Oct modeled smoke $PM_{2.5}$ can differ across inventories by $> 20 \mu g m^{-3}$ ($> 500\%$). Using the relative fire confidence metrics, we deduce that uncertainties in this region arise primarily from the small, fragmented fire landscape and very poor satellite observing conditions due to clouds and thick haze at this time of year. Indeed, we find that modeled smoke $PM_{2.5}$ using GFASv1.2, which adjusts for fires obscured by clouds and thick haze and accounts for peatland emissions, is most consistent with observations in Singapore, as well as in Malaysia and Indonesia. Finally, we develop an online app called FIRECAM for end-users of global fire emissions inventories. The app diagnoses differences in emissions among the five inventories and gauges the relative uncertainty associated with satellite-observed fires on a regional basis.

* Corresponding author.

E-mail address: tianjialiu@g.harvard.edu (T. Liu).

<https://doi.org/10.1016/j.rse.2019.111557>

Received 18 October 2018; Received in revised form 11 September 2019; Accepted 23 November 2019

0034-4257/ © 2019 The Authors. Published by Elsevier Inc. This is an open access article under the CC BY-NC-ND license (<http://creativecommons.org/licenses/by-nc-nd/4.0/>).

1. Introduction

1.1. Global fire emissions inventories: role in modeling studies and methodological differences

Models of atmospheric composition depend on global fire emissions inventories to reconstruct and project the impacts of biomass burning on air quality (Cusworth et al., 2018), public health (Crippa et al., 2016; Koplitz et al., 2016), climate (Rogers et al., 2015; Tosca et al., 2013), ecosystem dynamics (Yi et al., 2014), and land-atmosphere exchanges (Prentice et al., 2011). Many regional and global modeling studies consider only one global fire emissions inventory as input primarily to limit computational cost (Crippa et al., 2016; Kim et al., 2015; Koplitz et al., 2016; Maasackers et al., 2016; Marlier et al., 2019). End-users may simply choose an inventory based on spatio-temporal resolution, near-real-time availability, or keep the default inventory imposed in some chemical transport models (CTM). However, disagreements in the magnitude and temporal variability of emissions among inventories can significantly impact model estimates of variables relevant to air quality (Cusworth et al., 2018), public health (Koplitz et al., 2018b), or the budgets of atmospheric species (Heymann et al., 2017; Li et al., 2019; Shi et al., 2015; Zhang et al., 2014). Thus, it is important to understand the underlying causes for differences in both the magnitude and spatio-temporal variability of fire emissions in order to better inform fire prediction (Chen et al., 2017), land management decisions (Marlier et al., 2019), and other applications. While previous studies have identified regional discrepancies among various global fire emissions inventories (e.g., Li et al., 2019; Shi et al., 2015), here we also construct metrics to diagnose such discrepancies, and we present the online app FIRECAM to allow end-users to rapidly compare inventories across the globe and view the metrics.

Five global fire emissions inventories are widely used in modeling studies: (1) Global Fire Emissions Database (GFED; van der Werf et al., 2017), (2) Fire Inventory from NCAR (FINN; Wiedinmyer et al., 2011), (3) Global Fire Assimilation System (GFAS; Kaiser et al., 2012), (4) Quick Fire Emissions Dataset (QFED; Darmenov and da Silva, 2013), and (5) Fire Energetics and Emissions Research (FEER; Ichoku and Ellison, 2014) (Table 1). Estimates of fire emissions generally follow the “bottom-up” (e.g. GFED, FINN) or “top-down” approach (e.g. QFED, GFAS, FEER). In this study, we broadly define “bottom-up” as burned area-based and “top-down” as fire energy-based. The bottom-up burned area approach in GFED and FINN is based on MODIS burned area (MCD64A1) and/or active fire (MOD14, MYD14) products. It is important to note that even the bottom-up approach relies on active fire data: GFED has essentially become a hybrid product that ingests active fire locations for its small fire boost (Randerson et al., 2012), and the MCD64A1 algorithm itself is coupled with active fire data (Giglio et al., 2009). Fuel loadings, combustion completeness, and emissions factors, which are dependent on region and land use and land cover (LULC), are then used to convert burned area to fire emissions. Fuel loadings are derived from biogeochemical models (Hoelzemann et al., 2004; van der Werf et al., 2010), and combustion completeness is estimated as a function of soil moisture (van der Werf et al., 2017) or tree cover (Wiedinmyer et al., 2011). Emissions factors are compiled from lab experiments and vary by LULC (Akagi et al., 2011; Andreae and Merlet, 2001). The top-down approach in QFED, GFAS, and FEER uses fire energy from MODIS-derived fire radiative power (FRP), which is remotely sensed at top-of-atmosphere. Fire radiative energy (FRE), or the temporal integral of FRP, approximately linearly scales with the mass of dry matter (DM) consumed as fuel due to combustion (Wooster et al., 2005). Besides correcting for fires obscured by clouds in the top-down approach, GFAS, QFED, and FEER also use MODIS aerosol optical depth (AOD) to determine scaling factors for emissions of organic carbon (OC), black carbon (BC), and particulate matter < 2.5 μm in diameter ($\text{PM}_{2.5}$), which includes OC and BC (Darmenov and da Silva, 2013; Ichoku and Ellison, 2014; Kaiser et al., 2012).

To understand the causes for differences in fire emissions estimates, we first devise five “relative fire confidence metrics” based on major methodological differences between the five global inventories and factors that can affect satellite observing conditions: (1) type of input satellite fire dataset (i.e., burned area versus active fires), (2) cloud/haze obscuration of land surface, (3) burn extent and fragmentation, (4) variance in topography, and (5) additional small fires from VIIRS. We combine the five relative fire confidence metrics to map the relative fire confidence score for bottom-up emissions inventories primarily based on burned area (e.g. GFED) or active fire area (e.g. FINN). For top-down inventories, we estimate an FRP-based score to estimate the potential FRP enhancement from small fires below the MODIS detection limit, large fires not well-captured by the MODIS active fire product, and fires obscured by clouds and thick haze.

1.2. Regional case study: smoke exposure from fires in Indonesia

We then focus on Indonesia as a regional case study, as Indonesia can contribute a substantial fraction of annual global fire emissions. By some estimates, fires in Equatorial Asia, which mostly occur in Indonesia, account for 8% of carbon emissions from global fire activity on average, but as much as over a third during high fire intensity years (van der Werf et al., 2017). From incomplete combustion, fires release greenhouse gases and aerosols, including $\text{PM}_{2.5}$, and such emissions can trigger haze events, impacting visibility, air quality, climate, ecosystem services, and human health (Harrison et al., 2009; Page et al., 2009). Three main factors exacerbate haze episodes over Equatorial Asia: (1) synoptic meteorology, (2) fire-driven deforestation and agricultural management, and (3) carbon-rich peatlands in Indonesia (Marlier et al., 2019). First, during years with a strong El Niño and positive Indian Ocean Dipole phase, such as 2006 and 2015, suppression of convection over Indonesia leads to drought conditions (Crippa et al., 2016; Fernandes et al., 2017; Koplitz et al., 2016). Chen et al. (2017) found that a temporal cascade of pan-tropical fires, including large fires in Indonesia, is driven by the El Niño Southern Oscillation (ENSO) and changes in precipitation and terrestrial water storage. Second, small-holder farms and industrial concessions (oil palm, pulpwood, and rubber) are typically managed by fire to clear residues; forests are also cleared for agriculture and new plantations via burning (Dennis et al., 2005; Hoscilo et al., 2011; Marlier et al., 2015). Third, if the water table is low, peat fires can burrow underground and become extremely difficult to extinguish. Such fires can smolder for days to weeks, releasing substantial amounts of smoke into the atmosphere (Gras and Jensen, 1999; Hayasaka et al., 2014; Rein et al., 2008; van der Werf et al., 2008). Although fires occur every year in Indonesia (e.g., Koplitz et al., 2018a), the combination of these three natural and human-induced factors leads to especially severe haze over Equatorial Asia, such as in 1997, 2006, and 2015.

The high concentrations of $\text{PM}_{2.5}$ generated by fires in Equatorial Asia pose adverse health risks, leading to increased premature mortality. For example, Koplitz et al. (2016), Crippa et al. (2016), and Marlier et al. (2019) estimate 75,600–100,300 long-term premature adult deaths from cardiovascular and respiratory disease in Equatorial Asia due to the 2015 severe haze event. However, each of these studies differ in methodology, and specifically, in the global fire emissions inventory used: GFASv1.0 in Koplitz et al. (2016), FINNV2.0 in Crippa et al. (2016), and GFEDv4s in Marlier et al. (2019). In this study, we diagnose the impact of using different emissions inventories on estimates of population-weighted smoke exposures for Singapore, Indonesia, and Malaysia, following Koplitz et al. (2016) and Marlier et al. (2019).

1.3. Google Earth Engine: online platform for rapid geospatial analysis

In this study, we leverage Google Earth Engine (GEE; <https://earthengine.google.com>), an online platform for rapid geospatial

Table 1
Comprehensive comparison of the global fire emissions inventories for various methodological details and technical parameters. Broadly, we define “bottom-up” as burned area-based and “top-down” as fire energy-based inventories.

Inventory	GFEDv4s	FINNv1.5	GFASv1.2	QFEDv2.5f1	FEERv1.0-G1.2
	“Bottom-up”			“Top-down”	
Primary satellite fire input	MCD64A1 C5.1 burned area (500 m)	MCD14DL C5 active fire area (1 km)	MOD14/MYD14 C5/C6 FRP (1 km)	MOD14/MYD14 C6 FRP (1 km)	GFASv1.2 FRP (0.1°)
Spatio-temporal resolution	0.25°, monthly (daily fraction) 1997–2018 ^a	1 km, daily 2002–(NRT)	0.1°, daily 2003–(NRT)	0.1°, daily (0.25° × 0.375°, NRT) 2000–(NRT)	0.1°, daily 2003–(NRT)
Temporal range	Small fires boost 1997–2018 ^a	x	Cloud gap adjustment	QFED FRP- GFEDv2 DM global calibration	x
Statistical boosts	CASA biogeochemical model (van der Werf et al., 2010)	Hoelzemann et al. (2004)	GFAS FRP- GFEDv3 DM conversion factors by LULC	Applies global scaling constants for OC, BC, PM _{2.5} separately	Uses FRP-smoke AOD relationships to derive regional TPM emissions
Conversion to dry matter (DM) emissions	x	x	Recommends 3.4 global scaling	IGBP-INPE	MODIS IGBP dominant fire-prone LULC, 2004
Smoke AOD constraints for aerosol emissions	MCD12Q1 (UMD), annual	MCD12Q1 (IGBP), 2005	GFEDv3 dominant fire-prone LULC	(1 km)	(1°)
Primary land use/land cover (LULC)	(500 m)	(500 m)	(0.5°)	x	x
Peatland maps	Olson et al. (2001)	x	Same as GFED3 Heil et al. (2010)	Yes	x
Partitioning of emissions by LULC	Yes	Yes	x	Andreae and Merlet (2001)	Andreae and Merlet (2001) + updates from M.O. Andreae in 2014
Emissions factors	Akagi et al. (2011) + updates from M.O. Andreae in 2013	Akagi et al. (2011), Andreae and Merlet (2001)	from literature	Andreae and Merlet (2001)	Andreae and Merlet (2001) + updates from M.O. Andreae in 2014
Speciation	41 species	27 species	42 species	17 species	30 species
Ancillary products	Boosted BA, diurnal cycle, NPP	x	Cloud-gap adjusted FRP density, plume top/smoke injection altitude	Cloud-gap adjusted FRP density by LULC	x
References	van der Werf et al. (2017)	Wiedinmyer et al. (2011)	Kaiser et al. (2012)	Darmenov and da Silva (2013)	Ichoku and Ellison (2014)

NRT = near real time; CASA = Carnegie Ames Stanford Approach; UMD = University of Maryland; IGBP = International Biosphere-Geosphere Program; INPE = Instituto Nacional De Pesquisas Espaciais (Brazil's National Space Institute); NPP = Net Primary Production.

^a 2017–2018 are beta version releases.

analysis (Gorelick et al., 2017). Recently, GEE has been used in studies that require ease of access to satellite datasets and high computational power, such as for mapping crop yields (Azzari et al., 2017; Azzari and Lobell, 2017), trends in land use change (Kennedy et al., 2018), travel distance to cities (Weiss et al., 2018), and smoke exposure from fires (Marlier et al., 2019). Some of these studies also incorporate GEE's user interface capabilities, including Earth Engine Apps (<https://www.earthengine.app>) into online apps. Our use of GEE is two-fold: (1) to apply the relative fire confidence metrics at the global scale and (2) to use Earth Engine Apps to build the FIRECAM online tool.

The main objective of this study is to identify the methodological differences between five global fire emissions inventories and for end-users, show how these differences may lead to biases in results. To do so, we first use GEE to develop five relative fire confidence metrics to quantify some of the uncertainties. Next, we isolate the impact of using different inventories to estimate smoke exposure in Equatorial Asia from fires in Indonesia. Finally, we develop an online tool to help end-users to rapidly gauge the regional differences in emissions estimates and reduce potential biases in model results.

2. Methods

In this study, we use GEE to access and analyze satellite-derived datasets, many of which are already included in the GEE public data catalog. GEE couples a multi-petabyte-scale data catalog with cloud computing to make rapid geospatial analysis possible at scale (Gorelick et al., 2017). Use of GEE is thus critical to this study in order to apply the relative fire confidence metrics at a global scale and build the FIRECAM online tool.

2.1. Satellite fire datasets

We primarily use the Collection 6 (C6) satellite fire datasets from the MODIS sensors aboard the Terra and Aqua satellites, which have daily overpasses at $\sim 10:30$ am/pm and $\sim 1:30$ am/pm local time, respectively. These datasets are used in the construction of the five global fire emissions inventories considered here and publicly available from the NASA Earthdata catalog (<https://earthdata.nasa.gov/>). We analyze 15 years (2003–2017) of data from Collection 6 MCD64A1 burned area at monthly, 500-m spatial resolution (Giglio et al., 2018, 2009), MOD/MYD14A1 FRP and fire mask at daily, 1-km resolution (Giglio et al., 2016, 2003), and MCD14ML active fire geolocations also at daily, 1-km resolution. We hereafter refer to the Level-3 gridded active fire products MOD14A1 (Terra) and MYD14A1 (Aqua) collectively as MxD14A1 and Level-2 swath products as MxD14. We also use Collection 1 VNP14IMGML active fire geolocations, available since 2012, from the VIIRS sensor aboard the Suomi National Polar-orbiting Partnership (SNPP) satellite. VNP14IMGML is analogous to MCD14ML, but provides data at higher spatial resolution (375 m) and only during the Aqua overpass times (Schroeder and Giglio, 2017).

2.2. Relative fire confidence metrics

We devise five simple fire confidence metrics (ϕ) to assess the overall spatial variability and relative bias in global fire emissions inventories at $0.25^\circ \times 0.25^\circ$ spatial resolution and aggregated across 15 years (2003–2017) from monthly timesteps, as described below. Table 2 describes the satellite-derived datasets used. Then, as an example to end-users, we integrate the five metrics into more comprehensive “scores” to independently evaluate the spatial variability in uncertainty for bottom-up and top-down inventories. That is, we identify regions where each inventory may capture fire emissions either well or poorly, based on the five metrics.

- (1) **Spatial discrepancy between burned area and active fire area** (ϕ_{area}): we classify two main types of bottom-up emissions

inventories, based on the observations used to derive these inventories. For example, both GFED and FINN estimate burned area, but GFED uses the MCD64A1 burned area product, and FINN relies on MCD14ML active fire geolocations. MODIS burned area is typically classified based on the difference in the surface reflectance, or Normalized Burn Ratio (NBR), of pre-burn and post-burn images, while MODIS active fires are detected as “hotspots,” or thermal anomalies, each of which can be associated with areal extent to estimate burned area. To avoid confusion, we refer to burned area derived from MCD64A1 as $BA_{MCD64A1}$ or burned area (BA; as in GFED) and that from MxD14A1 as $BA_{MxD14A1}$ or “active fire area” (AFA; as in FINN). In contrast to the high threshold for the MCD64A1 burned area product, which reliably classifies burn scars > 1.2 km² (Giglio et al., 2006), the MxD14A1 active fire product can detect cool, smoldering fires more consistently and fires as small as 100 m² under clear-sky conditions (Giglio et al., 2003). However, burned area products may better capture short-lasting fires (sub-daily) and fires obscured by thick haze or clouds, since the burned area pre-burn versus post-burn algorithm is not limited by satellite overpass times (Giglio et al., 2009). The persistence of burn scars enables satellites to detect fires after clouds and haze have dissipated. To gauge the relative areal discrepancy of $BA_{MCD64A1}$ and $BA_{MxD14A1}$, we first aggregate $BA_{MCD64A1}$ to the 1-km spatial resolution of $BA_{MxD14A1}$. We then estimate total $BA_{MCD64A1}$ outside $BA_{MxD14A1}$ (BA_β) and $BA_{MxD14A1}$ outside $BA_{MCD64A1}$ (BA_α), over 2003–2017, and calculate the normalized difference index of BA_β and BA_α at $0.25^\circ \times 0.25^\circ$ spatial resolution:

$$\phi_{area} = \frac{\sum BA_\beta - \sum BA_\alpha}{\sum BA_\beta + \sum BA_\alpha} \quad (1)$$

where

$$BA_\beta = BA_{MCD64A1} - (BA_{MCD64A1} \cap BA_{MxD14A1}) \quad (2)$$

$$BA_\alpha = BA_{MxD14A1} - (BA_{MCD64A1} \cap BA_{MxD14A1}) \quad (3)$$

The range of the normalized difference index (-1 to $+1$) for the BA-AFA discrepancy indicates whether grid cells are either dominated by burned area (> 0) or active fire area (< 0). If either burned area or active fire area dominates (near -1 or $+1$), the datasets will not agree, and uncertainty is high. If the index is ~ 0 , the discrepancies between the datasets are minimal, wherein $BA_\beta \approx BA_\alpha$; in this case, however, the magnitude of BA_β and BA_α can vary while yielding similar index values.

- (2) **Cloud/haze effect on the ability of satellites to “see” fires** ($\phi_{cloud,haze}$): persistent cloud coverage and thick haze limit the opportunities for satellites to detect active fires or retrieve usable scenes for burned area classification. This metric diagnoses the fractional monthly cloud/haze burden at 500-m spatial resolution, weighted by FRP, but does not distinguish between smoke and cloud or varying cloud thickness and opacity. We use FRP rather than burned area since FRP is linearly related to DM emissions and more readily captures small fires (Wooster et al., 2005). We use the Collection 6 MODIS daily surface reflectance products MxD09GA and follow the algorithm proposed by Xiang et al. (2013) in each pixel, with “pixel” defined as one satellite observation in the native MODIS sinusoidal projection:

$$p_{cloud,haze} = \frac{\rho_1 - \rho_7}{\rho_1 + \rho_7} > 0 \text{ or } \rho_1 > 0.3 \quad (4)$$

where $p_{cloud,haze}$ refers to pixels designated as cloudy/hazy, ρ_1 indicates the MODIS surface reflectance in the 620–670 nm band (Red) and ρ_7 , the 2105–2155 nm band (SWIR-2). Cloudy and hazy pixels tend to be saturated in the visible bands relative to SWIR bands (Xiang et al., 2013). Pixels are classified as cloudy/hazy if either of the two criteria in Eq. (4) is met. We consider only those pixels with one or more active fire or burned area observations over the 2003–2017 timeframe to

Table 2

Satellite-derived datasets used for the five relative fire confidence metrics, which are described in Section 2.2.

Dataset	Description	Resolution	Satellite	Sensor	GEE ID
MCD64A1	Burned area	Monthly, 500 m	Terra/Aqua	MODIS	MODIS/006/MCD64A1
MOD14A1	Active fires	Daily, 1 km	Terra		MODIS/006/MOD14A1
MYD14A1			Aqua		MODIS/006/MYD14A1
MOD09GA	Surface reflectance	Daily, 500 m	Terra		MODIS/006/MOD09GA
MYD09GA			Aqua		MODIS/006/MYD09GA
MCD12Q1	Land cover	Yearly, 500 m	Terra/Aqua		MODIS/006/MCD12Q1
MCD14ML	Active fire geolocations	Daily, 1 km	Terra/Aqua		projects/GlobalFires/MCD14ML
VNP14IMGML		Daily, 375 m	S-NPP	VIIRS	projects/GlobalFires/VNP14IMGML
GMTED2010	Terrain elevation	2010 only, 7.5 arc sec	NGA's SRTM Digital Terrain Elevation Data		USGS/GMTED2010

NGA = National Geospatial-Intelligence Agency.

exclude misclassification of cloud/haze in snow, ice, and desert regions. After averaging the fraction of clouds and haze across $0.25^\circ \times 0.25^\circ$ grid cells, we weight the monthly fractional cloud/haze burden by FRP aggregated by month and satellite, over 2003–2017, to place more emphasis on the observing conditions during the months and hours of the diurnal cycle when fires are more likely to occur.

Like Xiang et al. (2013), MODIS also diagnoses clouds and haze but at coarser, 1-km resolution, which can result in overestimates of the cloud/haze fraction since clear pixels are mixed with cloudy or mixed cloudy pixels. However, the MODIS algorithm is better able than Xiang et al. (2013) to separate clouds or haze from bright surfaces such as snow/ice, desert, and built-up areas. We therefore use the FRP-weighted cloud/haze fraction derived from the MODIS algorithm to identify grid cells that may be misclassified as clouds due to the underlying bright surfaces. We assume that those pixels that MODIS characterizes as “cloudy” or having “mixed” clouds, cloud shadow, or high aerosol content are pixels obscured by cloud or haze. Then, for these grid cells, we check whether the FRP-weighted cloud/haze fraction derived from the Xiang et al. (2013) algorithm is positive. If yes, we use the FRP-weighted cloud/haze fraction from the MODIS algorithm for our metric.

(3) **Fragmentation and size of contiguous burned area** (ϕ_{fragment}): burned area products can better capture large, contiguous fires than small, fragmented fires due to the greater difference in NBR from pre-fire to post-fire and the persistence of burn scars on the land surface. On croplands, the small drop in NBR due to small fires can be conflated with harvest or masked by timely sowing of the next crop or by regrowth (e.g. Hall et al., 2016; Liu et al., 2019). In contrast, active fire products can generally detect such small, fragmented fires more accurately, so long as they occur during the satellite overpasses and are not obscured by clouds or haze. Dense clusters of small fires within a pixel can also increase the detection probability by enhancing the thermal anomaly or the NBR difference relative to background. For this metric, we estimate the total burned area and number of burn scar fragments over 2003–2017, using the average burned area per contiguous burn scar patch as a proxy for burn scar size and fragmentation. The *connectedComponents* function in GEE allows us to estimate the number of contiguous burn patches on a monthly basis at 500-m spatial resolution (Gorelick et al., 2017). To determine the connectivity of burn scars, we apply a circle kernel with a radius of 1 pixel; this assumes a “half neighbors” scheme, in which each pixel has 4 neighbors, and only pixels that share an edge are merged. One limitation of *connectedComponents* is that the algorithm limits the maximum number of pixels per patch at 256 pixels and identifies larger patches as background. We account for this limitation by increasing the total number of burn scar fragments in a grid cell by one if the MCD64A1 burned area is larger than the size of the patch derived by *connectedComponents*. Additionally, the $0.25^\circ \times 0.25^\circ$ grid used to extract the contiguous burn scars sets an upper bound

on burned area per patch for those large fires extending across multiple grid cells. Values $> 2 \text{ km}^2$ per burn fragment indicate large, contiguous fires, while small values represent small, fragmented fires.

- (4) **Roughness in topography** ($\phi_{\text{topography}}$): rough terrain, or large variances in local elevation, can inhibit active fire detection or burned area classification by introducing shadows, leading to insufficient background control pixels and artificial variations in surface reflectance (Fornacca et al., 2017). We estimate the neighborhood variance of terrain elevation as an indication of rough terrain. We use the U.S. Geological Survey (USGS) Global Multi-resolution Terrain Elevation Data 2010 (GMTED2010) at 7.5 arc sec ($\sim 250 \text{ m}$) spatial resolution, derived primarily from the Shuttle Radar Topography Mission (SRTM) Digital Terrain Elevation Data from the National Geospatial-Intelligence Agency (NGA). For each pixel, we estimate the neighborhood variance using a square kernel with a radius of 2 pixels. We then mask out water bodies using the 250-m MODIS/Terra land/water mask (MOD44W C6) and upscale the topography variance to $0.25^\circ \times 0.25^\circ$ spatial resolution by calculating the mean. Values close to 0 indicate flat topography, while values $> 1000 \text{ m}^2$ indicate rough, mountainous terrain. One limitation of this simple metric is that it does not account for terrain curvature, whose calculation is not yet supported by GEE.
- (5) **Additional small fires detected by VIIRS** (ϕ_{VIIRS_S}): VIIRS aboard S-NPP detects active fires at 375-m (I-bands) and 750-m (M-bands) spatial resolution in comparison to the 1-km spatial resolution of MODIS active fire detections (Schroeder and Giglio, 2017). The difference in spatial resolution suggests that VIIRS can detect smaller and cooler fires than MODIS. However, global fire emissions inventories have historically depended on MODIS since VIIRS is available only since 2012, or over a decade less than MODIS. While these additional small fires may comprise only a small portion of the global carbon budget, they can be important local point sources that contribute to regional air pollution. We approximate additional FRP observed by VIIRS at 375-m spatial resolution as the fractional FRP of VIIRS fires outside MODIS active fire and burned area pixels during the time period when the two satellite records overlap (2012–2017). Values range from 0 (no additional VIIRS FRP outside MODIS burn extent) to 1 (only VIIRS FRP).

2.2.1. Bottom-up inventories: relative fire confidence scores (BA-score, AFA-score)

Taken together, the five metrics described above capture the primary reliance on MODIS burned area (e.g., GFED) versus active fire (e.g., FINN) products as the base input satellite-derived fire dataset in a bottom-up approach and difficulty in the satellite detection of fires due to cloud/haze obscuration and limited spatial and temporal resolution. Using these five metrics, we estimate a relative fire confidence score for the two bottom-up emissions inventories, which are based on either burned area (as in GFED) or active fire area (as in FINN). For each

metric and each grid cell, we assign an initial integer confidence score ranging from 0 to 10, with 10 as highest confidence score, based on the decile distribution of all grid cells. Grid cells with only MODIS active fire, only MODIS burned area, or only VIIRS active fire observations are assigned the lowest confidence score of 0. We then average the scores from the fire confidence metrics in each grid cell and adjust the scale by setting the median score for the final relative fire confidence score for that grid cell to 0. This score represents the relative degree to which we can be confident in fire emissions for these inventories. We associate low cloud/haze burden, low variance in elevation, and low fraction of additional VIIRS fires with high confidence. To assess inventories based on burned area (e.g., GFED), we calculate a “BA-score,” in which high burned area outside active fire area (metric 1) and low burn fragmentation (metric 3) denote high confidence. For inventories based on active fires (e.g., FINN), we calculate an “AFA-score,” in which we reverse the scales for metrics 1 and 3 and place more relative confidence in grid cells dominated by active fire area over burned area and fragmented burn landscapes.

2.2.2. Top-down inventories: adjusted potential FRP adjustment (pFRP)

Top-down FRP-based inventories often include statistical cloud-gap adjustment and/or smoke AOD constraints, making them difficult to directly compare against the bottom-up inventories. Cloud-gap adjustments correct for fires blocked from satellite detection due to clouds or thick haze. These adjustments rely on data assimilation of previous observations and assumptions regarding fire persistence (Darmenov and da Silva, 2013; Kaiser et al., 2012). As an additional top-down constraint, fire emissions are scaled to match smoke-aerosol emissions derived from AOD observations (Ichoku and Ellison, 2014). We thus devise a separate score, the adjusted potential FRP enhancement (pFRP), or “FRP-score,” to assess the three top-down inventories (GFAS, QFED, FEER). The pFRP score diagnoses additional fire energy, unaccounted for by the MODIS active fires product but indicated by large burn scars from the MODIS burned area product or very small fires from the 375-m VIIRS active fires product. We first estimate the potential FRP enhancement as the sum of (1) fractional FRP inside MCD64A1 burned area extent but outside active fire area, over 2003–2017, and (2) fractional VIIRS FRP outside the combined extent of both MODIS burned area and active fire area, or metric 5, over 2012–2017. To obtain the adjusted potential FRP enhancement, we then multiply the potential FRP enhancement by the complement of the cloud/haze obscuration fraction, or metric 2. High pFRP values suggest low confidence in top-down inventories under clear-sky conditions.

2.3. Global fire emissions inventories

To convert burned area or FRP into emissions, fire emission inventories rely on estimates and assumptions regarding an array of variables as land cover type, fuel load, or emissions factors. Here we summarize these estimates and assumptions across five inventories (GFEDv4s, FINNv1.5, GFASv1.2, QFEDv2.5r1, and FEERv1.0-G1.2) over 2003–2016 and at both global and regional scale (Table 1). The versions of the inventories considered here are current as of 2018. We then compare the resulting emissions of carbon dioxide (CO₂), carbon monoxide (CO), methane (CH₄), OC, BC, and PM_{2.5} emissions from five global fire emissions inventories. Each inventory is described in more detail in Supplementary Section S2.

2.4. Modeling smoke PM_{2.5} from regional fire emissions

Following Kim et al. (2015) and Koplitz et al. (2016), we use the adjoint of the GEOS-Chem CTM to estimate the influence of upwind fires on smoke exposure at population-weighted receptors. We define smoke PM_{2.5} as the enhancement in PM_{2.5} due to fire activity. As used here, the GEOS-Chem adjoint maps the sensitivities of smoke PM_{2.5} at particular receptors to fire emissions in grid cells across a source region,

creating a footprint of such sensitivities. These footprints depend on the transport pathways from the source to the receptor and vary with meteorology. By multiplying these sensitivities by the different fire emissions inventories, we can easily compare estimates of monthly smoke PM_{2.5} exposure in Indonesia, Singapore, and Malaysia, from 2003 to 2016. We thus apply monthly adjoint sensitivities, which span a range of meteorology from 2005 to 2009, to the sum of OC and BC emissions, the main components of smoke PM_{2.5}. Due to the high computational cost of the GEOS-Chem adjoint, we match existing 2005–2009 sensitivities to each emissions year from 2003 to 2016 by determining the closest meteorological year in terms of rainfall (Kim et al., 2015; Koplitz et al., 2016). To do so, we use daily rainfall rates from Climate Hazards Group Infrared Precipitation with Station Data (CHIRPS; Funk et al., 2015), averaged temporally over the fire season and spatially over Sumatra and Kalimantan, Indonesia (Fig. S3). CHIRPS is a daily, 0.05° × 0.05° dataset that integrates both observational and satellite data to provide quasi-global rainfall data since 1981. As in Fernandes et al. (2017) and Marlier et al. (2019), we define the fire season in Indonesia as July to October.

Following Marlier et al. (2019), we further validate modeled smoke PM_{2.5} with ground observations in Singapore. We first extend the daily PM_{2.5} observations, available from 2014 to 2016, from the Singapore National Environment Agency (NEA) to 2010 by converting Pollution Standards Index (PSI) observations to PM_{2.5}. As used by the Singapore NEA, PSI is an air quality index that incorporates concentrations of six pollutants: CO, sulfur dioxide (SO₂), nitrogen dioxide (NO₂), ozone (O₃), PM₁₀, and PM_{2.5} (<https://www.haze.gov.sg/>). To further extend the record back to 2003, we train a multi-variate regression model of monthly mean NEA PM_{2.5} observations using visibility, air temperature, wind speed, and rainfall observations from the Singapore Changi airport, available from NOAA Global Summary of the Day (GSOD). The model yields an adjusted r^2 with observations of 0.94 (Fig. S5). We then reconstruct monthly PM_{2.5} for 2003–2016 and subtract the background PM_{2.5}, or the median PM_{2.5} (13.77 μg m⁻³) during non-fire season months (January to June and November to December), to obtain smoke PM_{2.5} for our validation. Validation for Malaysia and Indonesia is described in Supplementary Section S3.2.

3. Results

3.1. Spatial patterns in relative fire confidence metrics and scores

Overall, the five relative fire confidence metrics broadly differentiate: (1) large, continuous versus small, fragmented landscapes, (2) cloudy/hazy versus clear satellite observing conditions during the fire season, and (3) flat versus mountainous or rugged terrain. First, the map of BA-AFA discrepancies (metric 1) reveals the regions where the burned area BA_β and active fire area extent BA_α disagree. Regions dominated by high burned area outside the active fire area extent ($BA_\beta \gg BA_\alpha$) include the western Australia shrublands, sub-Saharan Africa savannas, and Kazakhstan and eastern Mongolia grasslands. Regions dominated by active fire area outside burned area extent ($BA_\beta \ll BA_\alpha$) are more widespread and primarily cover agricultural and/or mountainous areas (Fig. 1). Additionally, this metric highlights artificial discontinuities in the MODIS burned area product, most prominently north of the Black Sea, likely due to separate data processing for each MODIS tile (Giglio et al., 2018). Second, the FRP-weighted cloud/haze fraction (metric 2) shows that tropical and boreal forest regions, as well as eastern China, are conducive to poor satellite observing conditions due to cloud or haze during the fire season, with index values > 0.5 (Fig. 2). These areas with persistent cloud/haze burden are consistent with independent estimates of high mean cloud frequency (Wilson and Jetz, 2016) and are also co-located with high MODIS burn date uncertainty, indicating that many retrieved satellite scenes are unusable (Fig. S9). Third, the pattern of burn size and fragmentation (metric 3) is similar to that of the BA-AFA discrepancy:

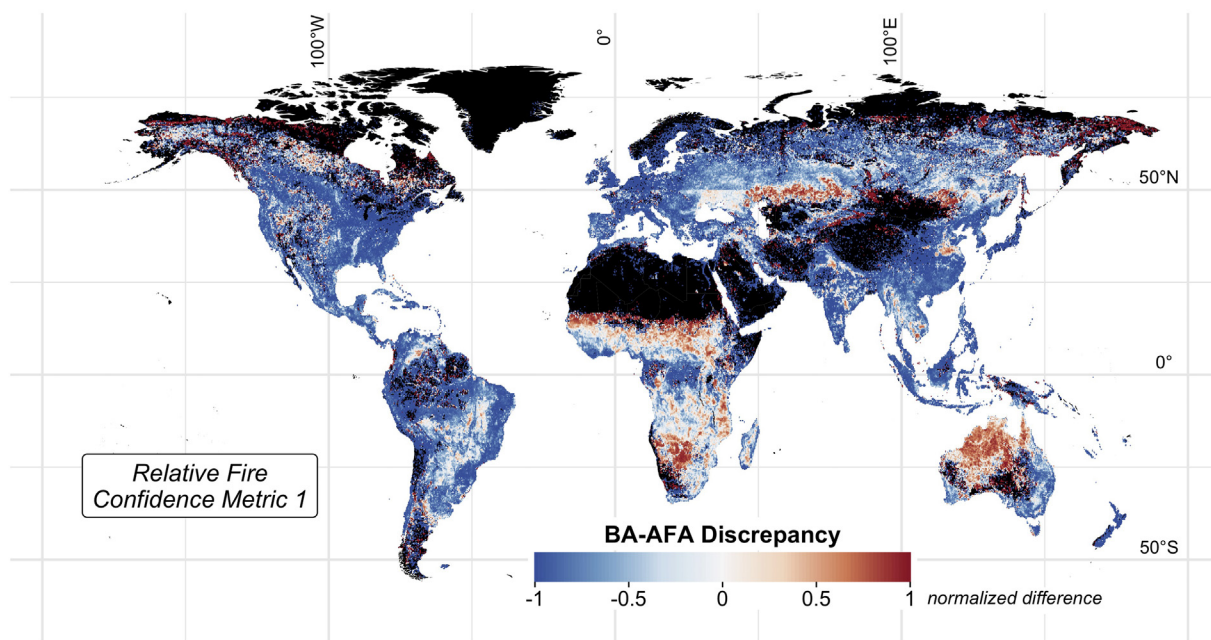


Fig. 1. Metric 1 for relative fire confidence score (ϕ_{area}): discrepancy between MCD64A1 burned area (BA) and Mxd14A1 active fire area (AFA) based on the normalized difference of BA outside AFA and AFA outside BA. Values are averaged over 2003–2017 and mapped at $0.25^\circ \times 0.25^\circ$ spatial resolution. High values (darker red) indicate relatively more confidence in BA than AFA, and low values (darker blue) the opposite. (For interpretation of the references to color in this figure legend, the reader is referred to the web version of this article.)

areas with large, contiguous fires are better captured by burned area, while areas with small, fragmented fires are better represented by active fire detections (Fig. 3). Our method for burn size/fragmentation yields spatial patterns consistent with fire size from the Global Fire Atlas, a catalog that characterizes over 13 million individual fires detected by MODIS (Andela et al., 2019). Fourth, topographical variance (metric 4) differentiates mountainous or rugged terrain, such as in western U.S. and southeast Asia, versus flat terrain, such as in northern India and western Australia (Fig. 4). Fifth, the map of VIIRS fires outside the MODIS burn extent (metric 5) reveals locations dominated by

small fires that are not well-detected by a coarser resolution sensor like MODIS (Fig. 5). In total, 38% of total VIIRS FRP does not overlap with the MODIS burn extent, revealing the importance of very small fires.

Taken together, the five metrics compose the relative fire confidence scores for bottom-up emissions inventories primarily derived from either burned area (BA-score; Fig. S1a), such as GFEDv4s, or active fire area (AFA-score; Fig. S1b), such as FINNv1.5. While the mapped BA-score and AFA-score mostly track the patterns of the large, contiguous fires versus small, fragmented fires, some areas exhibit low relative confidence (e.g., croplands in eastern China, tropical forests in

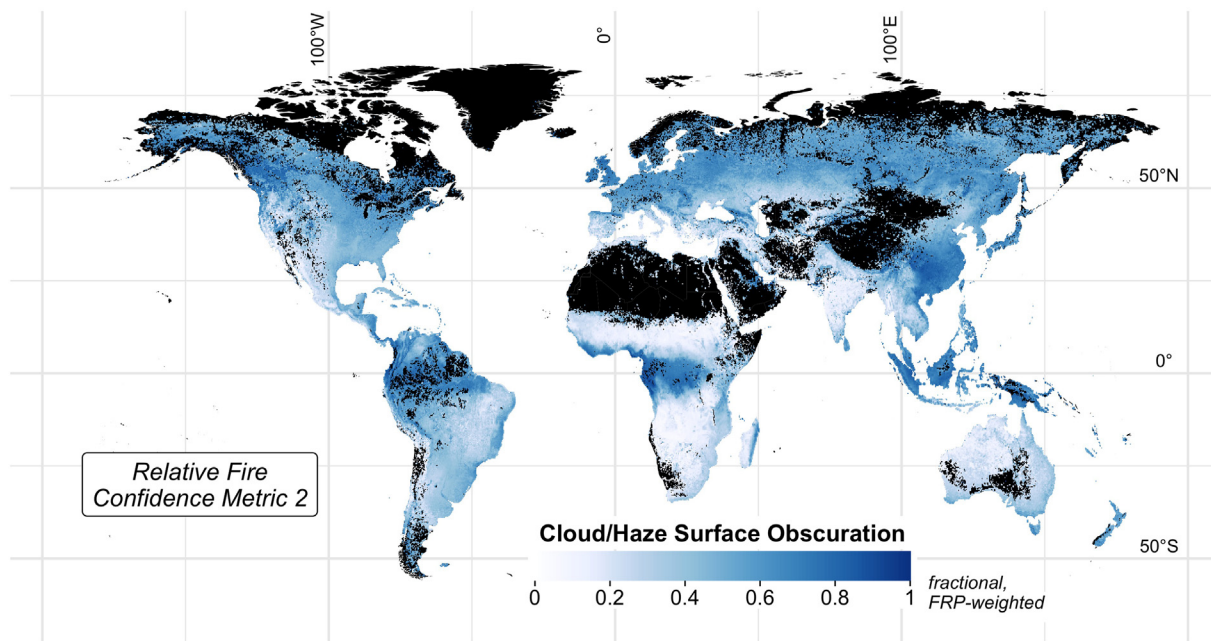


Fig. 2. Metric 2 for relative fire confidence score ($\phi_{cloud,haze}$): cloud/haze fraction based on MxD09GA surface reflectance and weighted by FRP. Values are averaged 2003–2017 and mapped at $0.25^\circ \times 0.25^\circ$ spatial resolution. High FRP-weighted cloud/haze fraction indicates fewer opportunities for satellite observation of the land surface during the fire season.

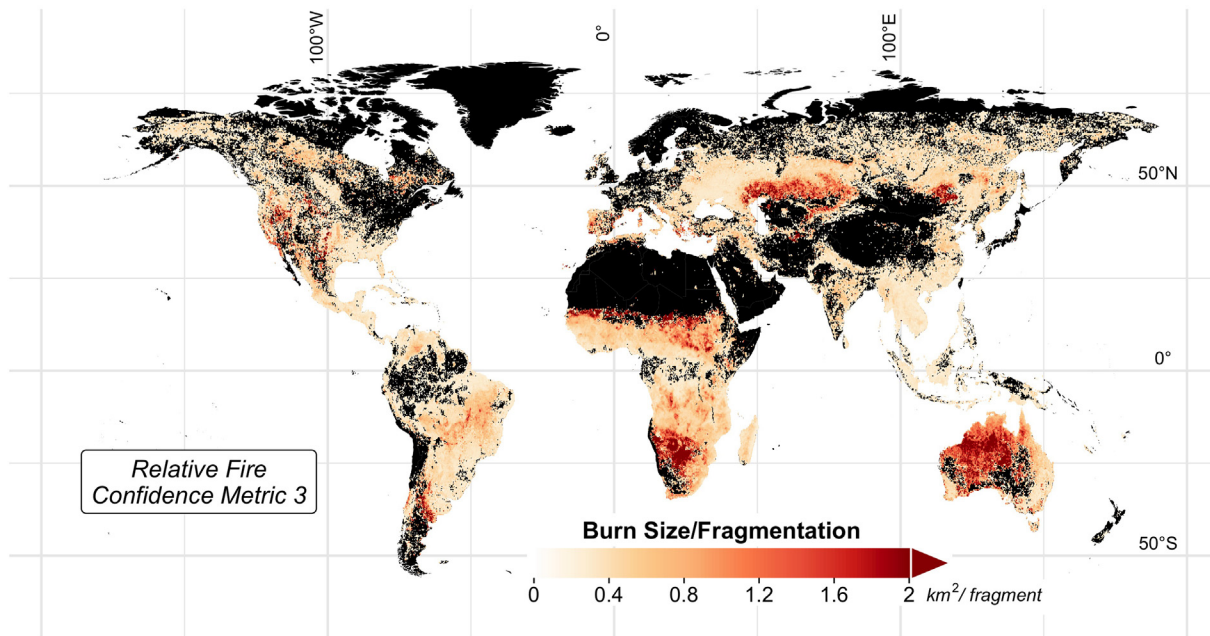


Fig. 3. Metric 3 for relative fire confidence score ($\phi_{fragment}$): average burned area (km^2) per “fragment,” or contiguous patch of burned area, averaged over 2003–2017 and mapped at $0.25^\circ \times 0.25^\circ$ spatial resolution. High values indicate dominance of large, contiguous fires; low values denote dominance of small, fragmented fires.

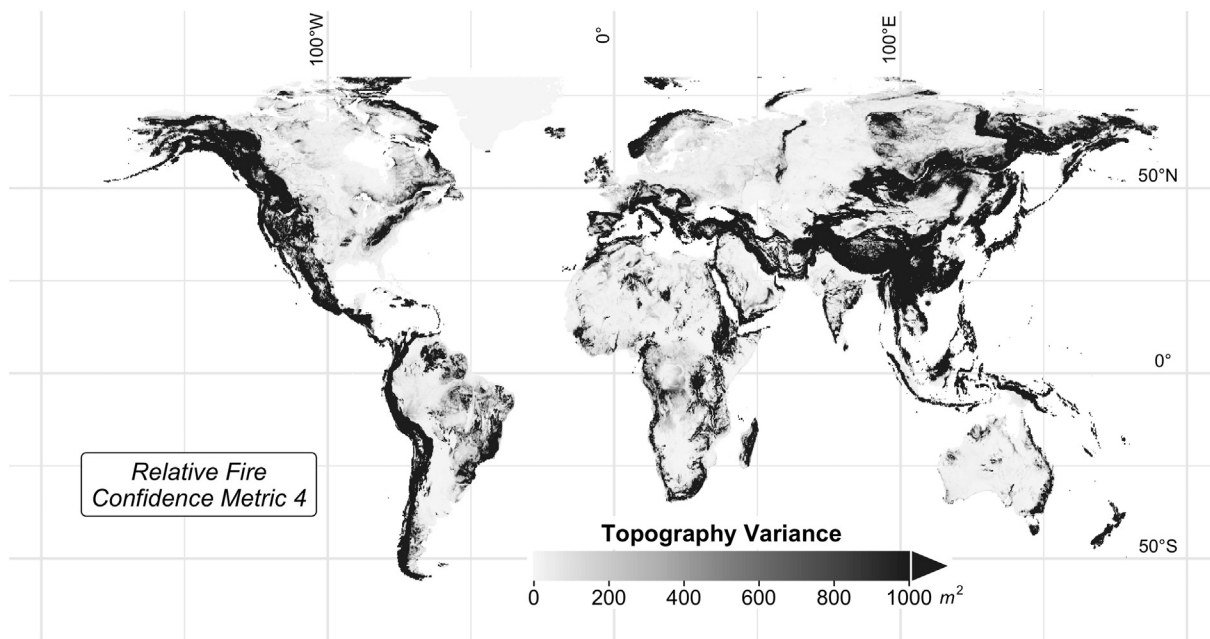


Fig. 4. Metric 4 for relative fire confidence score ($\phi_{topography}$): roughness in topography, expressed as variance in elevation (m^2), averaged over 2003–2017 and mapped at $0.25^\circ \times 0.25^\circ$ spatial resolution. High values in topography variance indicate steep gradients in elevation, or mountainous terrain, whereas low values indicate relatively flat terrain.

the Democratic Republic of Congo) or high relative confidence (e.g., tropical forests in central-southern Amazon, savannas in Botswana and Namibia) for both scores due to the effects of cloud/haze cover and/or topographical variance. Some caveats apply here. While we take the BA-score to apply to GFEDv4s, this inventory also boosts burned area using active fire counts to account for small fires. Additionally, for AFA-score, we assume an active fire area of 1 km^2 for all fires, while FINNv1.5 uses 0.75 km^2 for savanna and grassland fires and further scales the active fire area for all fires by the fractional vegetation cover of a given 1-km pixel (Wiedinmyer et al., 2011). Both GFEDv4s and FINNv1.5 rely on outdated MODIS products: GFEDv4s on MCD64A1

C5.1 burned area and FINNv1.5 on MCD14DL C5 active fires; however, for all our metrics, we use updated satellite products from MODIS C6 (MCD64A1 and MxD14A1). Despite our simplified approach and use of different versions of the satellite fire products, the normalized difference between GFEDv4s burned area and FINNv1.5 active fire area is spatially well-correlated with the BA-AFA discrepancy ($r = 0.59$, $p < 0.01$), or metric 1. We also find that the normalized difference between GFEDv4s and FINNv1.5 emissions for all six species is also moderately correlated with the BA-AFA discrepancy ($r = 0.53\text{--}0.57$, $p < 0.01$), confirming that the difference between GFEDv4s and FINNv1.5 emissions is related to the satellite fire input dataset used.

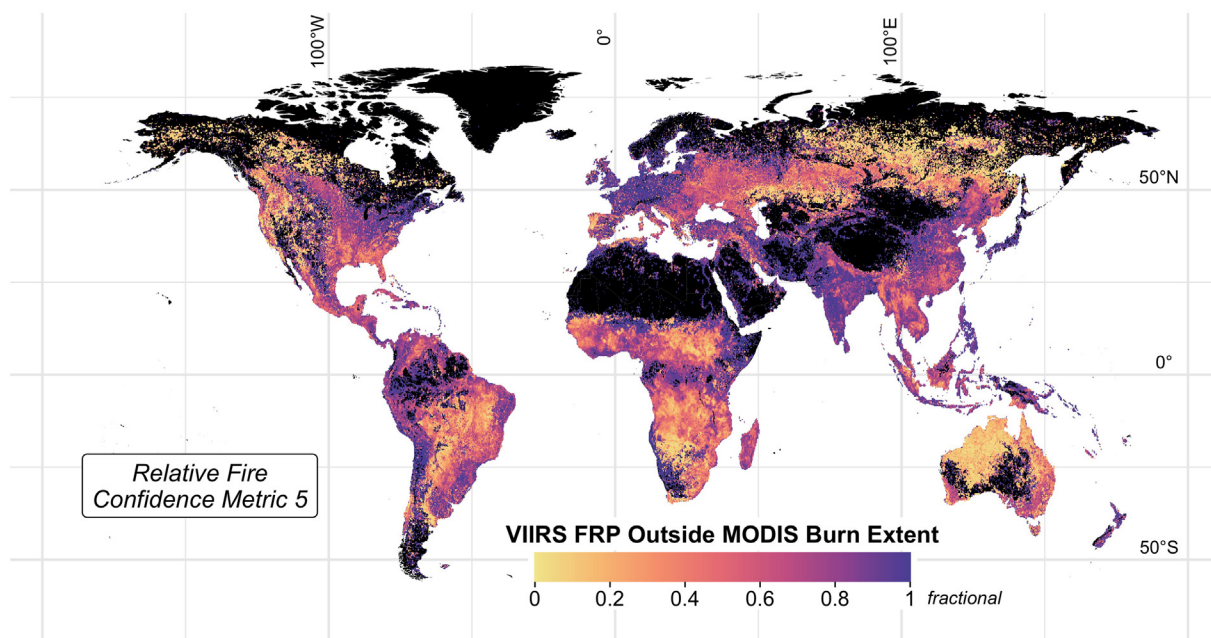


Fig. 5. Metric 5 for relative fire confidence score ($\phi_{VIIRS,sf}$): additional fires detected by VIIRS. Values are the areal fraction of VIIRS FRP occurring outside MODIS burned area and active fire pixel area, averaged over 2003–2017 and mapped at $0.25^\circ \times 0.25^\circ$ spatial resolution. A value of 0 indicates that all VIIRS active fires overlap MODIS active fires, and a value of 1 indicates the presence of VIIRS active fires but no MODIS burned area or active fire observations.

The pFRP metric assesses top-down FRP-based emissions inventories (GFAS, QFED, and FEER; Fig. S2). In total, we estimate 24% and 38% potential FRP enhancement from large fires (using MODIS BA) and very small fires (using VIIRS FRP), respectively, from 2003 to 2017. Put another way, the FRP-based inventories may be missing nearly two-thirds of fires under clear-sky conditions. Regions with low pFRP, and thus high uncertainty, include India and sub-Saharan Africa. In these regions, the low pFRP implies that either the satellite overpasses are missing a large number of short-lived or fast-spreading fires or the fires are too small to detect at coarse resolution. For example, the satellite overpasses at 10:30 am and 1:30 pm likely underestimate fire energy in the sub-tropics, where fire activity generally peak in the late afternoon (Giglio, 2007). Regions characterized by high cloud/haze cover during the fire season, such as tropical and boreal forests, have low pFRP due to our assumption that the cloud-gap corrections in these inventories successfully capture the fires obscured by clouds/haze.

3.2. Comparison of global fire emissions inventories: speciation and emissions factors

We find inconsistencies in the speciation of the overall emissions budget for CO_2 , CO, CH_4 , OC, BC, and $\text{PM}_{2.5}$ across the five global fire emissions inventories. For example, QFEDv2.5r1 and FEERv1.0-G1.2 estimate ~ 2 – 3 times as much OC, BC, and $\text{PM}_{2.5}$ emissions than the other inventories, with QFEDv2.5r1 higher than FEERv1.0-G1.2 (Table 3). Mean annual OC + BC emissions, from 2003 to 2016, among inventories differ by 5–126% in coefficient of variation (CV; Fig. 6). In regions with a high CV, such as temperate North America (102%) and the Middle East (126%), QFEDv2.5r1 OC + BC emissions are much higher than those from other inventories. These discrepancies shed light on the impact of the different algorithms that convert burned area or fire energy into aerosol emissions. For example, QFED and FEER apply top-down constraints on aerosol emissions to match smoke AOD, while such adjustments are absent in GFED, FINN, and GFAS. FEER uses smoke AOD to directly calculate TPM, which is then broken down into aerosol species, while QFED enhances aerosol emissions with a constant global scaling factor for each LULC (Darmenov and da Silva, 2013; Ichoku and Ellison, 2014). This global, rather than regional, AOD-based

scaling in QFED may explain the large CV in the Middle East and North America. Indeed, using MODIS/Aqua AOD, Darmenov and da Silva (2013) find significant variation in these scaling factors across each LULC – e.g., from 2–3 in tropical forest, 3–5 in extratropical forests, and 1–3 in grasslands and savannas.

To better understand the discrepancies across inventory emissions, we examine the emissions factors used in GFEDv4s and in earlier versions of FINN, GFAS, and QFED: FINNv1.0, GFASv1.0, and QFEDv2.4. We assume that emissions factors for the current versions of these three inventories do not deviate significantly from those in previous versions (Darmenov and da Silva, 2013; Kaiser et al., 2012; Wiedinmyer et al., 2011). First, we assess the impact of LULC classification on emissions factors by deriving a globally averaged emissions factor for each emitted species in each inventory, weighted by the total DM emissions for each LULC. To isolate the differences in LULC classification among inventories, we use the GFEDv4s DM emissions partitioned by LULC for the weighting. Since FINN subdivides the GFEDv4s savanna, grasslands, and shrublands LULC into two smaller LULC, we derive weights for these LULC using FINNv1.5 emissions. We find that the coefficients of variation in emission factors across the four inventories are relatively small for CO_2 , CO, OC, and BC (1.75–6.67%), compared to those for CH_4 and $\text{PM}_{2.5}$ (20.3–26.7%; Table 4). On average, GFEDv4s and GFAS, which consider peatlands as a separate LULC, have about 60% higher weighted mean emissions factors for CH_4 than FINN and QFED. This discrepancy arises because the peat emissions factor ($20.8 \text{ g CH}_4 \text{ kg}^{-1} \text{ DM}$) is ~ 2.5 – 14 times as high as CH_4 emissions factors for other LULC (Table S1), and only GFEDv4s and GFAS consider peatlands separately. In contrast to Li et al. (2019), we do not consider that FEERv1.0-G1.2 accounts for peatlands (Table 1), since FEER only uses the “permanent wetland” classification from the MODIS land cover product, which misses much of the peatland cover in Indonesia compared to the Olson et al. (2001) dataset used by GFED (van der Werf et al., 2017) and GFAS (Heil et al., 2010; Kaiser et al., 2012). The high CH_4 , as well as CO, emissions factors for peat fires can be attributed to incomplete combustion from smoldering fires, which are common in boreal and tropical peatlands (Kasischke and Bruhwiler, 2002; Stockwell et al., 2016). Additionally, the $\text{PM}_{2.5}$ emissions factors used in FINN for woody savanna/shrubland and savanna/grassland (8.3 – $15.4 \text{ g PM}_{2.5} \text{ kg}^{-1} \text{ DM}$)

Table 3

Average annual global CO₂, CO, CH₄, organic carbon (OC), black carbon (BC) and fine particulate matter (PM_{2.5}) emissions (Tg yr⁻¹, ± 1σ) by inventory, from 2003 to 2016. The percent difference in emissions relative to GFEDv4s is in brackets. For each species, the inventory with the highest emissions is denoted in bold font. The coefficient of variation (CV; %) indicates the spread of values, normalized by the mean, across the five inventories.

Species	Mean Annual Global Emissions (Tg)					CV (%)
	GFEDv4s	FINNv1.5	GFASv1.2	QFEDv2.5r1	FEERv1.0-G1.2	
CO ₂	6986 (595)	6362 (1025)	7083 (604)	7449 (665)	13,205 (1044)	34
	-	[-9%]	[+1%]	[+7%]	[+89%]	
CO	336 (39)	334 (54)	366 (43)	348 (31)	609 (52)	30
	-	[-1%]	[+9%]	[+4%]	[+81%]	
CH ₄	15 (3)	16 (3)	20 (3)	15 (1)	30 (3)	33
	-	[+8%]	[+35%]	[+2%]	[+103%]	
OC	16 (2)	20 (3)	19 (2)	47 (5)	30 (3)	48
	-	[+26%]	[+21%]	[+199%]	[+91%]	
BC	1.8 (0.2)	1.9 (0.3)	2.1 (0.2)	5.3 (0.5)	3.9 (0.3)	52
	-	[+8%]	[+15%]	[+196%]	[+119%]	
PM _{2.5}	35 (3)	31 (6)	31 (3)	74 (7)	51 (4)	39
	-	[+2%]	[-11%]	[+112%]	[+47%]	

are 16–214% higher than those used in GFEDv4s, GFAS, QFED (4.9–7.17 g PM_{2.5} kg⁻¹ DM) for the broader savanna, grassland, and shrubland LULC, which may explain the high PM_{2.5} weighted mean emissions factor for FINN (Table S1).

3.3. Modeling monthly smoke PM_{2.5} from Indonesia fires

We use monthly GEOS-Chem adjoint sensitivities, from 2005 to 2009, with the five global fire emissions inventories to model smoke PM_{2.5} in Singapore, Malaysia, and Indonesia from 2003 to 2016,

focusing on the impact of upwind Indonesian fires (Figs. 7–8, S7–8). According to GFEDv4s, peat fires contributed almost half of total OC + BC emissions in Indonesia from 1997 to 2016. Modeled monthly mean smoke PM_{2.5} is moderately to strongly correlated with observations (r = 0.64 to 0.84, p < 0.01), with GFASv1.2 smoke PM_{2.5} most closely matching the temporal variability of observed PM_{2.5} enhancement from smoke (Fig. 8a). We find similarly strong correlations for population-weighted smoke PM₁₀ in Malaysia (r = 0.54 to 0.89, p < 0.01) and satellite AOD in Indonesia (r = 0.63 to 0.93, p < 0.01; Figs. S7–S8). While the correlation of modeled and observed smoke

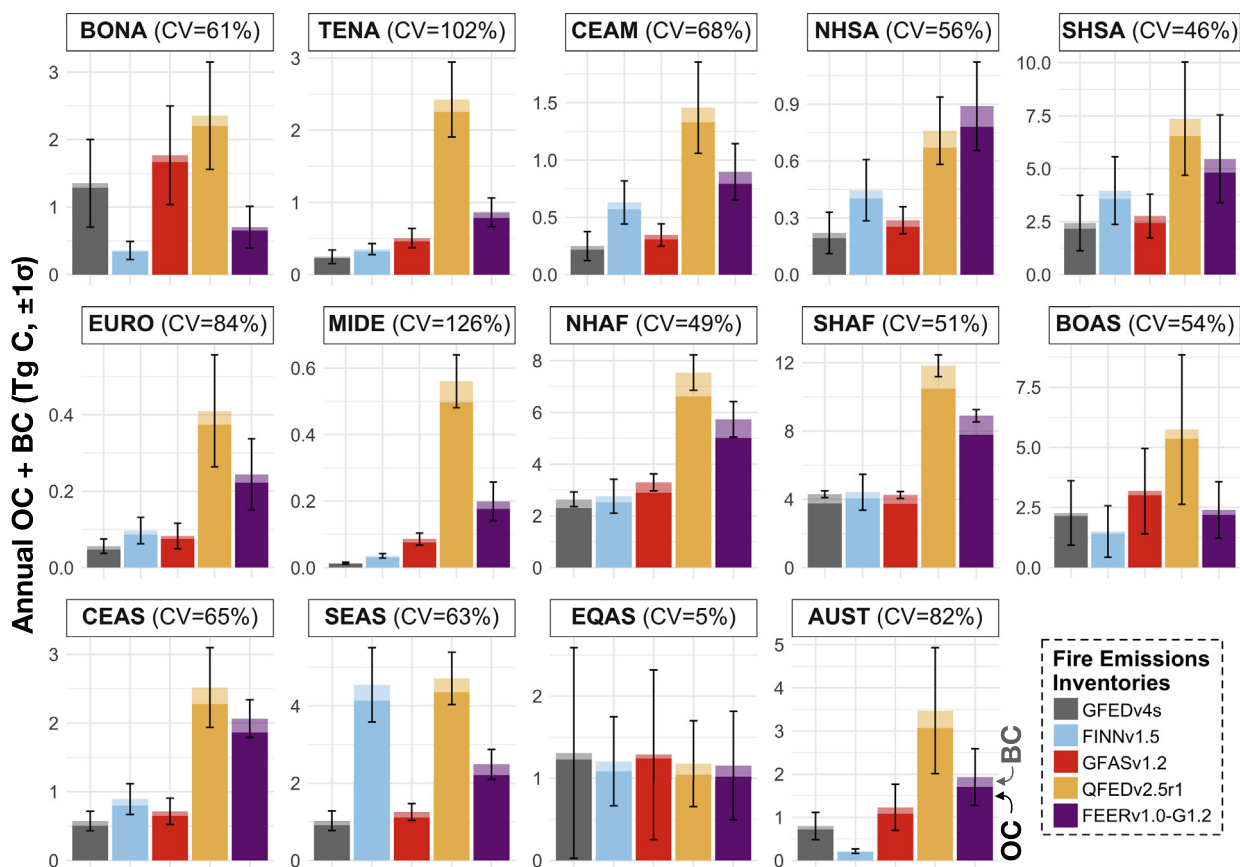


Fig. 6. Mean annual OC + BC emissions (Tg yr⁻¹, ± 1σ), over 2003–2016, from five global fire emissions inventories (GFEDv4s, FINNv1.5, GFASv1.2, QFEDv2.5r1, and FEERv1.0-G1.2) for the 14 GFEDv4s basis regions (Fig. S12; van der Werf et al., 2017). Acronyms for the 14 basis regions are given in Fig. S12. The fraction of OC emissions is denoted by darker shades, and that of BC emissions by lighter shades. Vertical bars show one standard deviation of the means over time. The coefficient of variation across inventories (CV, %) is shown for each region.

Table 4

Average emissions factors (g species kg⁻¹ dry matter) for CO₂, CO, CH₄, OC, BC and PM_{2.5}, weighted by fractional emissions over GFEDv4s land use and land cover (LULC). The coefficient of variation (CV; %) gives the variation, normalized by the mean, across inventories by species.

Species	Mean emissions factors (g species kg ⁻¹ dry matter), weighted by GFEDv4s LULC				CV (%)
	GFEDv4s	FINNv1.0	GFASv1.0	QFEDv2.4	
CO ₂	1648	1660	1611	1601	1.75
CO	95	87	91	84	5.45
CH ₄	6.67	4.43	7.1	4.2	26.7
OC	5.73	6.43	5.77	6.09	5.38
BC	0.47	0.46	0.49	0.53	6.67
PM _{2.5}	9.65	12.46	8.29	8.29	20.3

PM_{2.5} in Singapore is consistent across inventories, the magnitude of modeled smoke PM_{2.5} can differ by > 20 μg m⁻³ for the Jul-Oct average during extreme smoke episodes, such as in 2006 and 2015 (Fig. 8b). For example, the models yield mean Jul-Oct smoke PM_{2.5} concentrations in 2006 that differ from observed smoke by -64% to +70%. For the 2006, 2009, and 2015 high fire intensity years, modeled Jul-Oct smoke PM_{2.5} using GFASv1.2 yields the smallest mean absolute error relative to the observations (16%), compared to such errors from the other four inventories (39–66%).

3.3.1. 2006 and 2015 severe haze events

Kopplitz et al. (2016) used GFASv1.0 and the GEOS-Chem adjoint to investigate the public health effects of smoke from Indonesian fires in 2006 and 2015. These authors estimated over 150% higher premature mortality over Equatorial Asia in 2015 (100,300 excess deaths) than in 2006 (37,600 excess deaths). This suggests higher exposure to smoke and more prolonged fire activity, as well as drier El Niño conditions, in

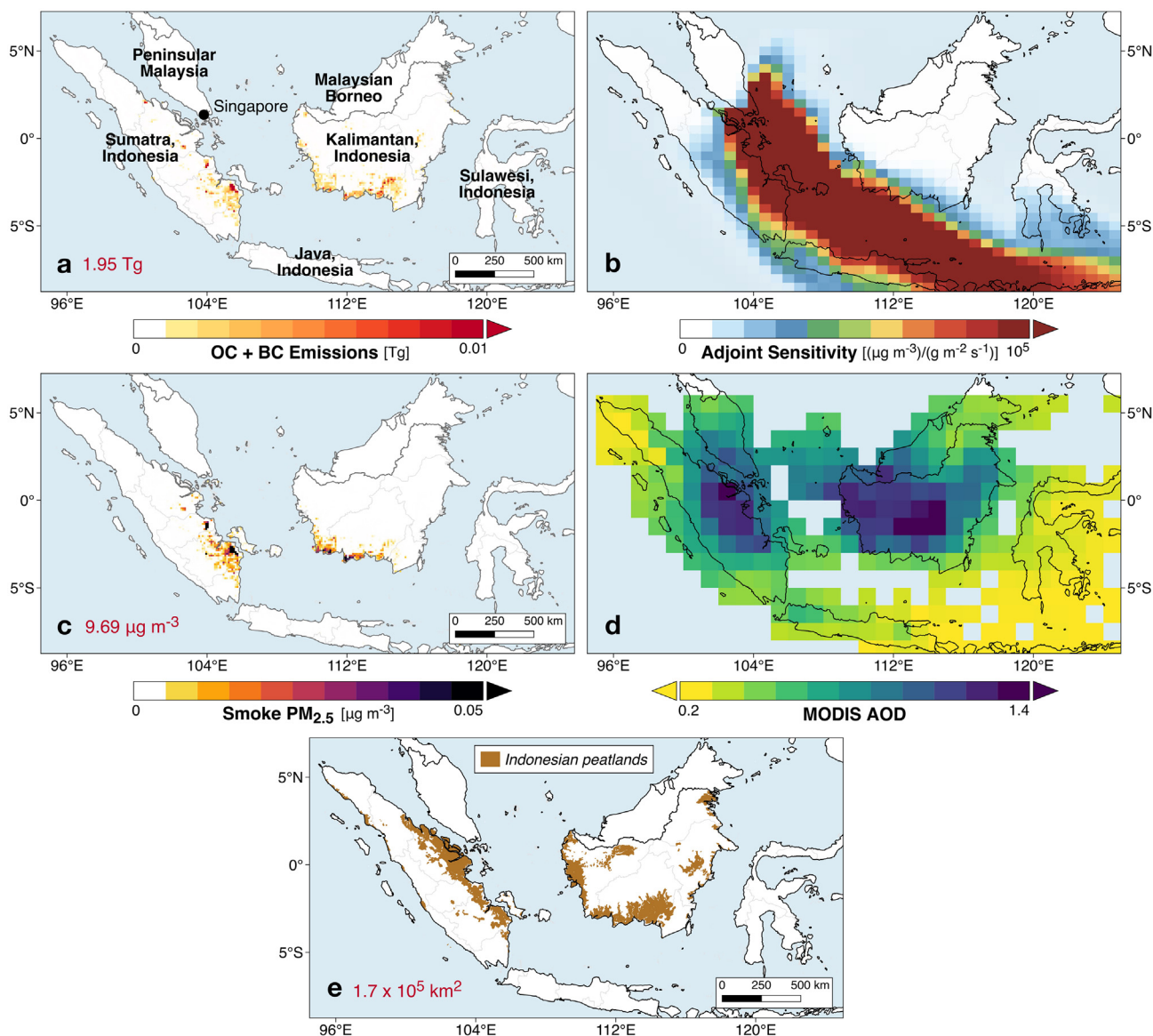


Fig. 7. Indonesia fires, smoke exposure in Singapore, and AOD in Equatorial Asia during July–October in 2006. (a) Total organic carbon (OC) and black carbon (BC) emissions from GFASv1.2. Sum of OC + BC fire emissions over Indonesia is shown inset. (b) Sensitivity of mean July–October smoke concentrations in Singapore to the location of fire emissions, calculated by the GEOS-Chem adjoint. (c) Contribution of smoke PM_{2.5} in Singapore from fires in individual grid cells over Indonesia, modeled using GFASv1.2 fire emissions. Average, calculated smoke PM_{2.5} exposure in Singapore, which is the sum of these contributions, is shown inset. (d) Average MODIS Terra and Aqua aerosol optical depth (AOD) in Equatorial Asia. (e) Distribution of peatlands in Sumatra and Kalimantan, Indonesia. The approximate total peatland area in these regions is shown inset.

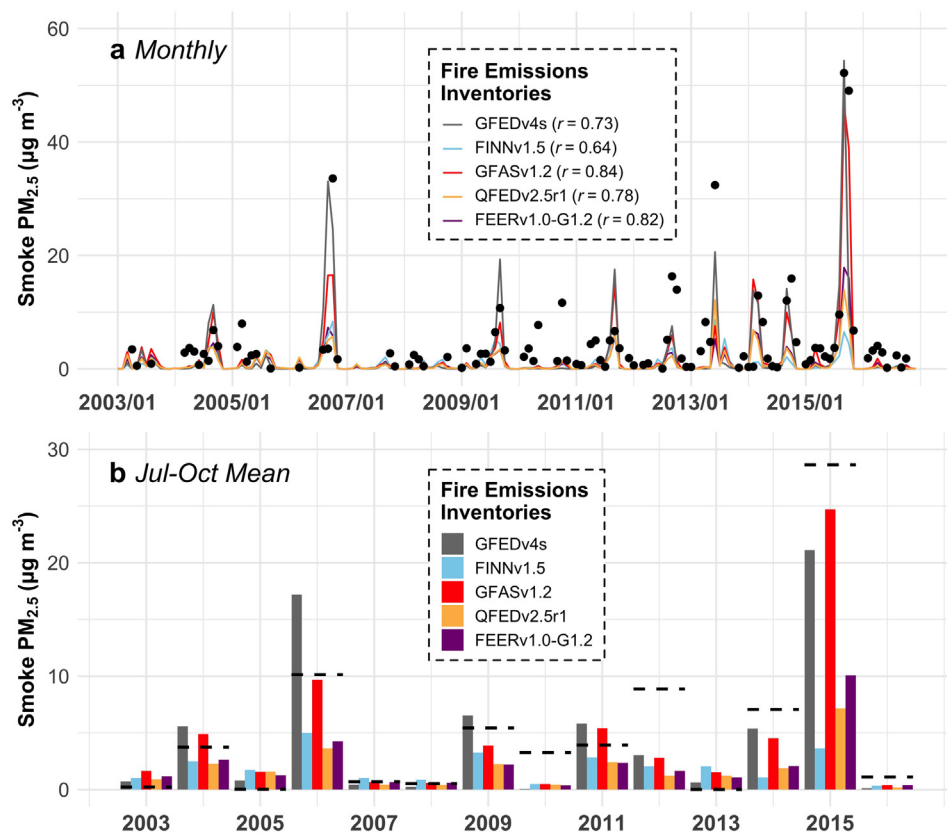


Fig. 8. Smoke PM_{2.5} exposure in Singapore, from 2003 to 2016. (a) Timeseries of monthly mean observed (black dots) and modeled (colored lines) smoke PM_{2.5} concentrations. Observed smoke PM_{2.5} is reconstructed from meteorological observations from the Singapore Changi Airport; only non-zero monthly smoke PM_{2.5} observations are shown. Modeled values are from the GEOS-Chem adjoint using different global fire emissions inventories: GFEDv4s, FINNv1.5, GFASv1.2, QFEDv2.5r1, and FEERv1.0-G1.2. Correlations between observed and modeled smoke PM_{2.5} are shown inset for each inventory and are statistically significant ($p < .01$). (b) Jul-Oct mean smoke PM_{2.5} by inventory, with observed smoke PM_{2.5} indicated by dashed horizontal lines. (For interpretation of the references to color in this figure legend, the reader is referred to the web version of this article.)

2015 compared to 2006. In this study, we first compare relative changes in modeled Jul-Oct mean smoke exposure in Singapore between the 2006 and 2015 fire seasons. In addition, the strong negative exponential relationship between rainfall and metrics of fire activity (e.g., active fire count, burned area) in Indonesia is well-established (Fernandes et al., 2017; van der Werf et al., 2017). However, Eck et al. (2019) suggest that thick smoke may obscure fires from satellite detection. To determine whether fire activity in Equatorial Asia is under-detected in 2015 due to haze, we first model the linear relationship between rainfall and fire activity, as well as with satellite AOD, in the log-log space for the 2003–2016 period. We use Jul-Oct rainfall rates from CHIRPS and MxD08_M3 AOD. As measures of seasonal mean fire activity, we use the MxD14A1 active fire mask, MxD14A1 FRP, and MCD64A1 burned area, averaged over the Indonesian provinces of Sumatra and Kalimantan, where most fires are concentrated. We then predict 2015 fires in the context of the log-log linear regression of rainfall and fires, modeled excluding 2015 observations. If fires are under-detected due to haze in 2015, then active fire counts, FRP, and burned area should deviate negatively from the modeled log-log rainfall-fire relationships, compared to AOD, which should not deviate significantly.

Several phenomena indicate a more severe haze episode in 2015 than in 2006. The Niño 3.4 index, which is a proxy for ENSO and based on anomalies in tropical Pacific sea surface temperatures, suggests a stronger El Niño in 2015 than in 2006 (Koplitz et al., 2016). In addition, lower rainfall rates (−29%) and higher AOD (+31–34%) over Sumatra and Kalimantan in 2015 suggest drier and hazier conditions over these fire-prone regions, relative to 2006. In contrast, minimal increases in active fire count (+6%) and FRP (+10%) in 2015 relative to the long-term MODIS record, and even decreases in burned area (−35%) suggest that increased haziness in 2015 may have obscured many fires, making satellite detection of fires challenging. During the Indonesia fire season (Jul-Oct), satellite-observed smoke AOD and indicators of fire activity strongly correlate with rainfall in log-log space over 2003–2016 when

2015 is excluded ($r = -0.87$ to -0.98 , $p < 0.01$; Fig. 9). Given these relationships with rainfall, the 2015 fire activity appears severely underestimated, with active fire 60% less than expected, burned area 93% less, and FRP 62% less. In contrast, AOD in 2015 does not deviate significantly (−12%) from the modeled log-log relationship with rainfall.

The observed AOD and FRP in 2015 are within the 95% prediction interval for these variables, but both burned area and active fire counts are outside this interval. We now examine how these potential underestimates in 2015 fire activity may have affected the fire emissions inventories. We find that GFEDv4s, which includes a small fires boost, and FINNv1.5, which uses active fires to estimate burned area, less severely underestimate (63–76%) burned area in 2015 than the MODIS burned area product (Fig. S4). Inventories that make cloud-gap adjustments for obscured fires are better able to discern the more severe haze event in 2015 and match the observed enhancement of 183% in smoke PM_{2.5} in Singapore: GFASv1.2 shows a 155% increase in smoke PM_{2.5} relative to 2006, and QFEDv2.5r1 and FEERv1.0-G1.2 yield increases of 96–137% (Fig. 8b). In contrast, GFEDv4s and FINNv1.5 do not capture the enhanced smoke PM_{2.5} in Singapore in 2015. Overall, GFASv1.2 most accurately captures both the magnitude and temporal variability of observed smoke PM_{2.5}, while FINNv1.5 consistently underestimates smoke PM_{2.5} in high fire intensity years and most poorly captures the temporal variability of observed smoke PM_{2.5}.

4. Discussion and conclusion

4.1. Relative fire confidence metrics: spatial patterns

The goal of this study has been to quantify and interpret differences across five bottom-up and top-down global fire emission inventories. While it is difficult to directly compare bottom-up and top-down inventories, end-users may use the relative confidence indicated by the BA-score, AFA-score, and FRP-score (pFRP) to select a “best” inventory

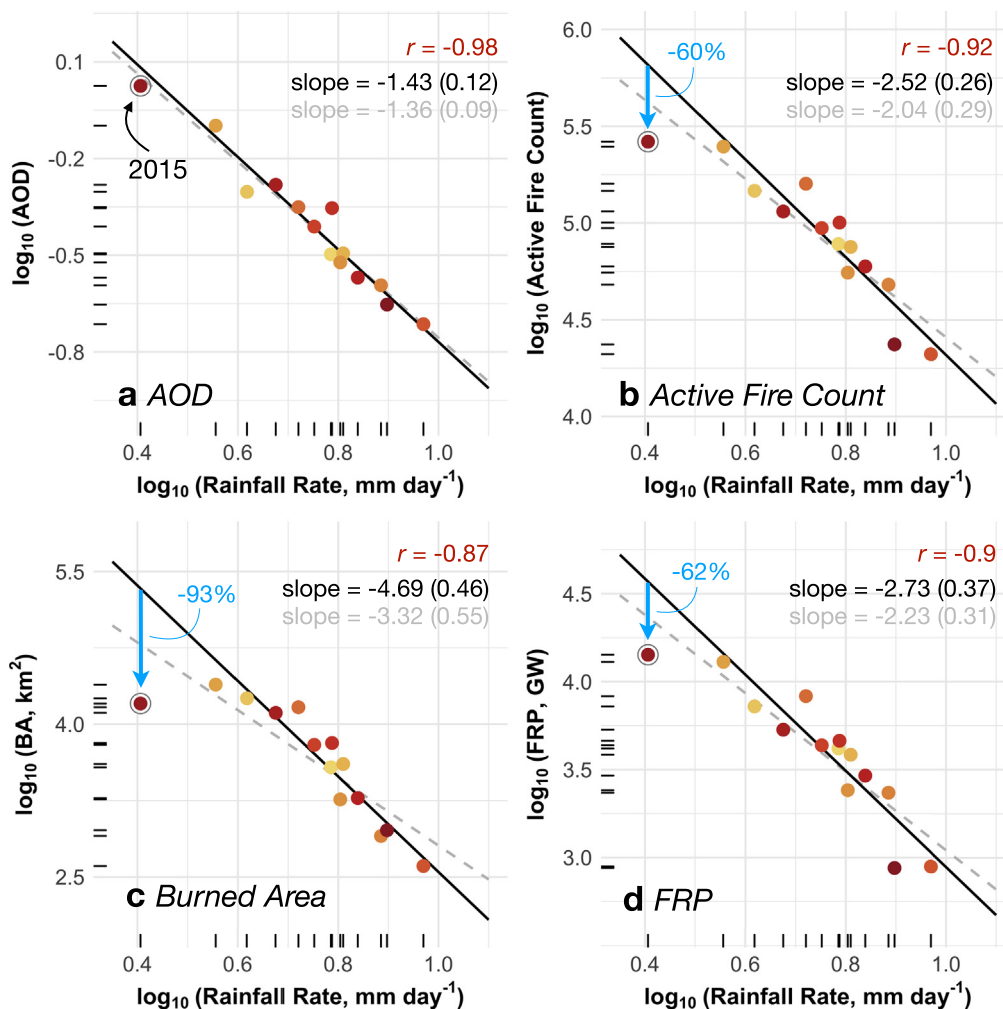


Fig. 9. Under-detection of 2015 Indonesia fires in MODIS active fire and burned area products relative to the 2003–2016 period. CHIRPS rainfall rates (mm day^{-1}) are plotted against MODIS (a) aerosol optical depth, (b) active fire count, (c) burned area (km^2), and (d) FRP (GW) in log-log space. All variables are averaged temporally over July–October and spatially over Sumatra and Kalimantan, Indonesia. Colors denote different years from 2003 to 2016, with later years depicted by redder shades; values for 2015 are circled. Inset shows the correlation (r , $p < 0.01$), slope of the linear regression (gray dashed line), and slope with 2015 removed (black line) for each pair of observations. Standard errors for the slopes are shown in parentheses. There is no statistically significant linear trend in any variable over time. Blue arrows in (b), (c), and (d) show that observed fires are lower than expected based on prediction from the linear regression of rainfall and fires that excludes 2015 observations. Percent underestimate of each fire variable based on these predictions is shown in blue. (For interpretation of the references to color in this figure legend, the reader is referred to the web version of this article.)

if limited by computing resources. Nevertheless, these simple scores represent just one way for end-users to evaluate the metrics together; end-users, for example, may choose to assess the five relative fire confidence metrics individually. One important limitation is that the relative fire confidence metrics are time-averaged and therefore do not fully account for interannual or seasonal variability in fire activity. However, in constructing these metrics, we have placed greater weight on high fire intensity years and the dominant fire-prone months in order for end-users to diagnose the overall spatial biases among inventories. Another caveat is that we do not investigate in as much detail the spatial differences in inventory-specific LULC, which affect the fuel consumption and emissions factors imposed.

We first find that two fire landscapes – large and cohesive versus small and fragmented – account for broad differences in the bottom-up fire emissions inventories, GFED and FINN. GFED, which relies primarily on observed burned area, better captures emissions from large, cohesive fires, while FINN, which depends on observed active fires, better captures emissions from small, fragmented fires. Second, the presence of thick cloud/haze during peak fire activity makes satellite fire detection more difficult in equatorial regions, boreal regions, and eastern China. Third, fires located in mountainous regions are also challenging to detect, especially by moderate-resolution sensors, such as MODIS (500 m or 1 km) or VIIRS (375 m or 750 m). For top-down fire emissions inventories (e.g., GFAS, QFED, and FEER), we calculate a pFRP score, which indicates potential underestimates in FRP under clear-sky conditions. We find high pFRP scores suggest that areas dominated by fast-spreading, large fires or short-lived, small fires under clear-sky conditions are not well-captured by MODIS due to limited

overpasses or moderate spatial resolution.

4.2. Regional application: validation of modeled smoke $\text{PM}_{2.5}$ across Equatorial Asia from Indonesia fires

Here we discuss the application of the relative fire confidence metrics for Indonesia fires. (Additional examples for the contiguous United States and northwestern India are discussed in Supplementary Section S6.) We do not explicitly consider the influence of spatial resolution in applying these fire emissions datasets. We focused on regional scale, so this influence is likely diluted. However, we acknowledge that spatial resolution may be important at local scale.

We can first deduce that fire-prone regions in Indonesia generally follow the small, fragmented fire landscape pattern (metrics 1, 3, and 5) and that high cloud cover and/or haze (metric 2) may impede observation during the fire season. While metric 4 shows rough terrain in parts of Indonesia (e.g., western Sumatra, Java, and northern Kalimantan), most fires occur on flat terrain. However, smoldering peat fires even on flat land may also be difficult to detect.

First, we find that thick haze in very high fire intensity years, such as 2015, likely leads to lower-than-expected fire activity derived from satellite observations. The AFA-score suggests high relative confidence for FINN, in contrast to the low relative confidence by BA-score for GFED; pFRP shows low potential FRP enhancement over Indonesia, primarily because of the presence of thick clouds or haze. Our results suggest that the 93% burned area underestimate in Indonesia arises primarily due to thick haze, an effect greater than the effect of such haze on active fire count (–60%) or FRP (–62%). For Singapore, as

well as for Malaysia and Indonesia, we find that top-down inventories yield modeled smoke $PM_{2.5}$ concentrations that are more consistent with observed $PM_{2.5}$ than bottom-up inventories, with $r = 0.78\text{--}0.84$ for top-down versus $r = 0.64\text{--}0.73$ for bottom-up inventories. This result is likely due to the cloud-gap adjustments in the top-down inventories.

Second, only GFAS and GFED consider peatlands as a separate LULC, while in other inventories, peatlands may be classified as savanna, tropical forest, or cropland. These discrepancies have implications for emissions since the carbon-rich peatlands are associated with high fuel load (van der Werf et al., 2010). While the moderate to strong correlation of observed and modeled smoke $PM_{2.5}$ is consistent across inventories, the magnitude of mean Jul-Oct smoke $PM_{2.5}$ in the high fire intensity years of 2006 and 2015 can vary by $> 20 \mu\text{g m}^{-3}$, with GFEDv4s and GFASv1.2 best capturing the magnitude of observed smoke $PM_{2.5}$ and yielding higher smoke $PM_{2.5}$ than the other three inventories. Additionally, estimated ratios of peat OC/BC emissions factors ratios are ~ 150 compared to just 3–39 for the other LULC types, thereby affecting the composition of smoke $PM_{2.5}$. Indeed, GFEDv4s and GFASv1.2 show 78–380% higher Jul-Oct OC/BC ratios over Sumatra and Kalimantan during 2003–2016 than the other three inventories. In summary, GFASv1.2, which adjusts for cloud gaps in satellite observations of fires and considers peatlands as a separate LULC class, performs best in terms of modeling smoke $PM_{2.5}$ that is consistent with observations in both temporal variability and magnitude.

4.3. Uncertainties in global fire emissions inventories

The uncertainties in global fire emissions inventories influence estimates of emissions budgets, the spatio-temporal variability of fires, and fire trends, with different inventories leading to different conclusions (Supplementary Section S7). Here we discuss the main sources of uncertainty in inventories: small fires, cloud gap adjustments, aerosol emissions enhancements, and emissions factors and LULC classification. Sole reliance on burned area from MCD64A1 may capture large, contiguous fires well but not the spatial allocation of small fires in fragmented burn landscapes. This is demonstrated by the moderate spatial correlation ($r = 0.36$, $p < 0.01$) between the BA-AFA discrepancy (metric 1) and burn size/fragmentation (metric 3). Additional VIIRS FRP detected outside the MODIS active fire extent (metric 5) also implies low confidence in areas dominated by small fires. As an example of low confidence in small fires, we find that many grid cells in GFEDv4s would not have any emissions without the small fires boost. Approximately one-fourth of grid cells with nonzero GFEDv4s fire emissions from 2003 to 2016 persistently show 100% spatial coverage by small fires, and the small fire boost alone contributes all the emissions in 57% of GFEDv4s grid cells, on average. Zhang et al. (2018) recommended that grid cells with only small fire contribution, or no MCD64A1 burned area input, be treated with caution. For example, these authors found that GFEDv4s significantly overestimates DM fuel consumption and emissions for areas with infrequent but small fires in eastern China during summer months. Under such conditions, when no burned area is detected, the scaling parameters applied to the total active fire count are not specific to individual grid cells and instead are averaged across regions, seasons, and land cover types (van der Werf et al., 2017).

On the other hand, because MODIS retrieves thermal anomalies only during satellite overpass times, use of MCD14ML active fires in the bottom-up inventories, as well as MxD14 FRP in the top-down inventories, may lead to underestimates of burned area and fire energy from large, contiguous fires. In addition, the FINN emissions inventory may overrepresent small fire emissions due to the assumption that at least 75% of the nominal pixel area is burned (Wiedinmyer et al., 2011). The active fire product also has coarser resolution and a lower detection threshold compared to the burned area product. Using FRP may address this overestimate since small fires are cooler and exhibit

lower FRP. Nonetheless, the dependence of the top-down inventories on GFED to convert FRP to DM burned may lead to underestimates of small fire emissions, as seen in the case of agricultural fire emissions in northwestern India (Cusworth et al., 2018).

The cloud/haze fraction (metric 2) indicates that regions with persistent cloud cover or thick haze during the fire season, such as boreal and tropical regions, degrade the quality of satellite observations of fire activity. By adjusting for cloud gaps and scaling with observed AOD, the top-down inventories – GFASv1.2, QFEDv2.5r1 and FEERv1.0-G1.2 – may be better able to match observations than the bottom-up inventories in these regions (Kopplitz et al., 2018b). However, the scaling factor of 3.4 recommended by Kaiser et al. (2012) for GFAS aerosol emissions, as well as the simple global QFED scaling by LULC, may bias regional smoke exposure estimates (e.g., Kopplitz et al., 2016) due to spatial variations in AOD scaling (Darmenov and da Silva, 2013; Ichoku and Ellison, 2014). We thus recommend comparison of aerosol emissions from QFEDv2.5r1 to FEERv1.0-G1.2, which directly estimates TPM using smoke AOD by region. Further, QFED calibrates the coefficient β relating FRP to DM globally, while GFAS uses LULC-specific β coefficients, which vary from 0.13 to 5.87 kg DM MJ⁻¹ FRP (Kaiser et al., 2012). We also show that certain species, such as CH₄, are greatly affected by LULC classification within the inventories, and in particular, by the treatment of peatland emissions. In our case study of Indonesian fires, GFEDv4s and GFASv1.2, both of which account for peatlands, yield much higher smoke $PM_{2.5}$ more in line with observations than the other three inventories. Finally, coarse-resolution LULC maps (0.5°–1°), which are used in GFASv1.2 and FEERv1.0-G1.2, may also bias emissions due to differences in fuel loadings in regions with more heterogeneous LULC, such as in Southeast Asia (Fig. S10b).

4.4. Future directions and recommendations

Integration of both burned area and active fire products into fire emission inventories may reduce underestimation of fires in small and fragmented or large and contiguous fire regions, respectively. Similar to the hybrid approach of using active fires for the small fire boost in GFEDv4s, incorporation of burned area in FINN could retroactively improve emissions estimates for large fires. For the top-down inventories of GFAS, QFED, and FEER, use of burned area as a secondary input satellite fire dataset may yield emissions more closely matched with observations compared to the current dependence on assumptions of fire persistence across cloud gaps and satellite overpasses. Standardization of emissions factors, in particular in the partitioning of LULC, could help reduce inconsistencies between inventories. In particular, the peatland maps used, if any, are incomplete and could be improved using more comprehensive global peatland datasets, such as PEATMAP (Xu et al., 2018). We also expect that the updated MODIS MCD12Q1 land cover dataset from C5 to C6 will lead to some differences between current and future emissions estimates (Sulla-Menashe et al., 2019). Further, access to high spatial resolution surface reflectance datasets from Landsat (30 m, every 16 days) and Sentinel-2 (20 m, every 5 days) in the GEE data catalog makes feasible both ground truth validation and improvement of burned area estimates and LULC classifications (Casu et al., 2017). Recent studies have shown overall improvement in accuracy and small burn scar detection using Landsat and Sentinel, but low revisit times may limit this improvement in areas with high cloudiness and rapid land use change (Crowley et al., 2019; Goodwin and Collett, 2014; Hawbaker et al., 2017; Roteta et al., 2019).

For end-users, we recommend use of multiple bottom-up and top-down inventories, if possible. Further, end-users should be aware that outdated emissions estimates can persist in models, leading to biases and errors in model results (Supplementary Section S8). We present here an online tool, “Fire Inventories: Regional Evaluation, Comparison, and Metrics” (FIRECAM; <https://globalfires.earthengine.app/view/firecam>), that allows users to compare regional monthly and

yearly emissions, from 2003 to 2016, from the five global inventories for six species (CO, CO₂, CH₄, OC, BC, and PM_{2.5}) and to interpret the regional differences between fire emissions by using the five relative fire confidence metrics (Fig. S11, Supplementary Section S5). FIRECAM will be updated regularly in the foreseeable future as new versions of the inventories and underlying datasets become available. We identify three key factors that should influence the end-user's inventory selection and can also significantly affect the results of modeling studies: input satellite fire dataset, statistical adjustments, and LULC classification and emissions factors. For example, in our case study on Indonesian fires, we find that the cloud-gap adjustment and representation of peatland emissions are two important factors that distinguish different inventories in the regional validation of smoke PM_{2.5}; both factors are included in the GFAS inventory. FIRECAM allows users to rapidly assess such differences in regional fire emissions.

Code availability

R and Google Earth Engine code for the FIRECAM tool and relative fire confidence metrics can be accessed from <https://github.com/tianjialiu/FIRECAM>.

Acknowledgements

T. Liu is funded by a NSF Graduate Research Fellowship (NSF grant DGE1745303). We acknowledge the Singapore National Environment Agency (NEA) and Malaysian Department of Environment (DOE) for maintaining a network of stations that provide continuous air quality measurements across Singapore and Malaysia. This research was partly funded by the US Environmental Protection Agency (EPA) grants 83587501 and 83587201. It has not been formally reviewed by the EPA. The views expressed in this document are solely those of the authors and do not necessarily reflect those of the EPA.

Appendix A. Supplementary data

Supplementary data to this article can be found online at <https://doi.org/10.1016/j.rse.2019.111557>.

References

- Akagi, S.K., Yokelson, R.J., Wiedinmyer, C., Alvarado, M.J., Reid, J.S., Karl, T., Crouse, J.D., Wennberg, P.O., 2011. Emission factors for open and domestic biomass burning for use in atmospheric models. *Atmos. Chem. Phys.* 11, 4039–4072. <https://doi.org/10.5194/acp-11-4039-2011>.
- Andela, N., Morton, D.C., Giglio, L., Paugam, R., Chen, Y., Hantson, S., van der Werf, G.R., Randerson, J.T., 2019. The Global Fire Atlas of individual fire size, duration, speed, and direction. *Earth Syst. Sci. Data* 11, 529–552. <https://doi.org/10.5194/essd-2018-89>.
- Andreae, M.O., Merlet, P., 2001. Emissions of trace gases and aerosols from biomass burning. *Glob. Biogeochem. Cycles* 15, 955–966. <https://doi.org/10.1029/2000GB001382>.
- Azzari, G., Lobell, D.B., 2017. Landsat-based classification in the cloud: an opportunity for a paradigm shift in land cover monitoring. *Remote Sens. Environ.* 202, 64–74. <https://doi.org/10.1016/j.rse.2017.05.025>.
- Azzari, G., Jain, M., Lobell, D.B., 2017. Towards fine resolution global maps of crop yields: testing multiple methods and satellites in three countries. *Remote Sens. Environ.* 202, 129–141. <https://doi.org/10.1016/j.rse.2017.04.014>.
- Casu, F., Manunta, M., Agram, P.S., Crippen, R.E., 2017. Big remotely sensed data: tools, applications and experiences. *Remote Sens. Environ.* 202, 1–2. <https://doi.org/10.1016/j.rse.2017.09.013>.
- Chen, Y., Morton, D.C., Andela, N., van der Werf, G.R., Giglio, L., Randerson, J.T., 2017. A pan-tropical cascade of fire driven by El Niño/Southern Oscillation. *Nat. Clim. Chang.* 7, 906–911. <https://doi.org/10.1038/s41558-017-0014-8>.
- Crippa, P., Castruccio, S., Archer-Nicholls, S., Lebron, G.B., Kuwata, M., Thota, A., Sumin, S., Butt, E., Wiedinmyer, C., Spracklen, D.V., 2016. Population exposure to hazardous air quality due to the 2015 fires in Equatorial Asia. *Sci. Rep.* 6, 1–9. <https://doi.org/10.1038/srep37074>.
- Crowley, M.A., Cardille, J.A., White, J.C., Wulder, M.A., 2019. Multi-sensor, multi-scale, Bayesian data synthesis for mapping within-year wildfire progression. *Remote Sens. Lett.* 10, 302–311. <https://doi.org/10.1080/2150704x.2018.1536300>.
- Cusworth, D.H., Mickley, L.J., Sulprizio, M.P., Liu, T., Marlier, M.E., DeFries, R.S., Guttikunda, S.K., Gupta, P., 2018. Quantifying the influence of agricultural fires in northwest India on urban air pollution in Delhi, India. *Environ. Res. Lett.* 13, 044018. <https://doi.org/10.1088/1748-9326/aab303>.
- Darmenov, A.S., da Silva, A., 2013. The Quick Fire Emissions Dataset (QFED) - Documentation of Versions 2.1, 2.2, and 2.4. 32 NASA Technical Report Series on Global Modeling and Data Assimilation.
- Dennis, R.A., Mayer, J., Applegate, G., Chokkalingam, U., Colfer, C.J.P., Kurniawan, I., Lachowski, H., Maus, P., Permana, R.P., Ruchiat, Y., Stolle, F., Suyanto, Tomich, T.P., 2005. Fire, people and pixels: linking social science and remote sensing to understand underlying causes and impacts of fires in Indonesia. *Hum. Ecol.* 33, 465–504. <https://doi.org/10.1007/s10745-005-5156-z>.
- Eck, T.F., Holben, B.N., Giles, D.M., Slutsker, I., Sinyuk, A., Schafer, J.S., Smirnov, A., Sorokin, M., Reid, J.S., Sayer, A.M., Hsu, N.C., Shi, Y.R., Levy, R.C., Lyapustin, A., Rahman, M.A., Liew, S.C., Salinas Cortijo, S.V., Li, T., Kalbermatter, D., Keong, K.L., Yuggotomo, M.E., Aditya, F., Mohamad, M., Mahmud, M., Chong, T.K., Lim, H.S., Choon, Y.E., Deranadyan, G., Kusumaningtyas, S.D.A., Aldrian, E., 2019. AERONET remotely sensed measurements and retrievals of biomass burning aerosol optical properties during the 2015 Indonesian Burning Season. *J. Geophys. Res. Atmos.* 124, 4722–4740. <https://doi.org/10.1029/2018JD030182>.
- Fernandes, K., Verchot, L., Baethgen, W., Gutierrez-Velez, V., Pinedo-Vasquez, M., Martius, C., 2017. Heightened fire probability in Indonesia in non-drought conditions: the effect of increasing temperatures. *Environ. Res. Lett.* 12, 054002. <https://doi.org/10.1088/1748-9326/aa6884>.
- Fornacca, D., Ren, G., Xiao, W., 2017. Performance of three MODIS fire products (MCD45A1, MCD64A1, MCD14ML), and ESA Fire_CCI in a mountainous area of Northwest Yunnan, China, characterized by frequent small fires. *Remote Sens.* 9, 1131. <https://doi.org/10.3390/rs9111131>.
- Funk, C., Peterson, P., Landsfeld, M., Pedreros, D., Verdin, J., Shukla, S., Husak, G., Rowland, J., Harrison, L., Hoell, A., Michaelsen, J., 2015. The climate hazards infrared precipitation with stations - a new environmental record for monitoring extremes. *Sci. Data* 2, 1–21. <https://doi.org/10.1038/sdata.2015.66>.
- Giglio, L., 2007. Characterization of the tropical diurnal fire cycle using VIRS and MODIS observations. *Remote Sens. Environ.* 108, 407–421. <https://doi.org/10.1016/j.rse.2006.11.018>.
- Giglio, L., Descloitres, J., Justice, C.O., Kaufman, Y.J., 2003. An enhanced contextual fire detection algorithm for MODIS. *Remote Sens. Environ.* 87, 273–282. [https://doi.org/10.1016/S0034-4257\(03\)00184-6](https://doi.org/10.1016/S0034-4257(03)00184-6).
- Giglio, L., Csizsar, I., Justice, C.O., 2006. Global distribution and seasonality of active fires as observed with the Terra and Aqua Moderate Resolution Imaging Spectroradiometer (MODIS) sensors. *J. Geophys. Res. Biogeosci.* 111, 1–12. <https://doi.org/10.1029/2005JG000142>.
- Giglio, L., Loboda, T., Roy, D.P., Quayle, B., Justice, C.O., 2009. An active-fire based burned area mapping algorithm for the MODIS sensor. *Remote Sens. Environ.* 113, 408–420. <https://doi.org/10.1016/j.rse.2008.10.006>.
- Giglio, L., Schroeder, W., Justice, C.O., 2016. The collection 6 MODIS active fire detection algorithm and fire products. *Remote Sens. Environ.* 178, 31–41. <https://doi.org/10.1016/j.rse.2016.02.054>.
- Giglio, L., Boschetti, L., Roy, D.P., Humber, M.L., Justice, C.O., 2018. The collection 6 MODIS burned area mapping algorithm and product. *Remote Sens. Environ.* 217, 72–85. <https://doi.org/10.1016/j.rse.2018.08.005>.
- Goodwin, N.R., Collett, L.J., 2014. Development of an automated method for mapping fire history captured in Landsat TM and ETM+ time series across Queensland, Australia. *Remote Sens. Environ.* 148, 206–221. <https://doi.org/10.1016/j.rse.2014.03.021>.
- Gorelick, N., Hancher, M., Dixon, M., Ilyushchenko, S., Thau, D., Moore, R., 2017. Google Earth Engine: planetary-scale geospatial analysis for everyone. *Remote Sens. Environ.* 202, 18–27. <https://doi.org/10.1016/j.rse.2017.06.031>.
- Gras, J.L., Jensen, J.B., 1999. Some optical properties of smoke aerosol in Indonesia. *Geophys. Res. Lett.* 26, 1393–1396.
- Hall, J.V., Loboda, T.V., Giglio, L., McCarty, G.W., 2016. A MODIS-based burned area assessment for Russian croplands: mapping requirements and challenges. *Remote Sens. Environ.* 184, 506–521. <https://doi.org/10.1016/j.rse.2016.07.022>.
- Harrison, M.E., Page, S.E., Limin, S.H., 2009. The global impact of Indonesian forest fires. *Biologist* 56, 156–163.
- Hawbaker, T.J., Vanderhoof, M.K., Beal, Y.-J., Takacs, J.D., Schmidt, G.L., Falgout, J.T., Williams, B., Fairaux, N.M., Caldwell, M.K., Picotte, J.J., Howard, S.M., Stitt, S., Dwyer, J.L., 2017. Mapping burned areas using dense time-series of Landsat data. *Remote Sens. Environ.* 198, 504–522. <https://doi.org/10.1016/j.rse.2017.06.027>.
- Hayasaka, H., Noguchi, I., Putra, E.I., Yulianti, N., Vadrevu, K., 2014. Peat-fire-related air pollution in Central Kalimantan, Indonesia. *Environ. Pollut.* 195, 257–266. <https://doi.org/10.1016/j.envpol.2014.06.031>.
- Heil, A., Kaiser, J.W., van der Werf, G.R., Wooster, M.J., Schultz, M.G., van der Gon, H.D., 2010. Assessment of the Real-time Fire Emissions (GFASv0) by MACC, ECMWF Technical Memo No. 626.
- Heymann, J., Reuter, M., Buchwitz, M., Schneising, O., Bovensmann, H., Burrows, J.P., Massart, S., Kaiser, J.W., Crisp, D., 2017. CO₂ emission of Indonesian fires in 2015 estimated from satellite-derived atmospheric CO₂ concentrations. *Geophys. Res. Lett.* 44, 1537–1544. <https://doi.org/10.1002/2016GL072042>.
- Hoelzemann, J.J., Schultz, M.G., Brasseur, G.P., Granier, C., Simon, M., 2004. Global Wildland Fire Emission Model (GWEM): evaluating the use of global area remote satellite data. *J. Geophys. Res. D Atmos.* 109. <https://doi.org/10.1029/2003JD003666>.
- Hosco, A., Page, S.E., Tansey, K.J., Rieley, J.O., 2011. Effect of repeated fires on land-cover change on peatland in southern Central Kalimantan, Indonesia, from 1973 to 2005. *Int. J. Wildland Fire* 20, 578–588. <https://doi.org/10.1071/WFI0029>.
- Ichoku, C., Ellison, L., 2014. Global top-down smoke-aerosol emissions estimation using satellite fire radiative power measurements. *Atmos. Chem. Phys.* 14, 6643–6667. <https://doi.org/10.5194/acp-14-6643-2014>.

- Kaiser, J.W., Heil, A., Andreae, M.O., Benedetti, A., Chubarova, N., Jones, L., Morcrette, J.J., Razinger, M., Schultz, M.G., Suttie, M., van der Werf, G.R., 2012. Biomass burning emissions estimated with a global fire assimilation system based on observed fire radiative power. *Biogeosciences* 9, 527–554. <https://doi.org/10.5194/bg-9-527-2012>.
- Kasischke, E.S., Bruhwiler, L.P., 2002. Emissions of carbon dioxide, carbon monoxide, and methane from boreal forest fires in 1998. *J. Geophys. Res.* 108, 8146. <https://doi.org/10.1029/2001JD000461>.
- Kennedy, R.E., Yang, Z., Gorelick, N., Braaten, J., Cavalcante, L., Cohen, W.B., Healey, S., 2018. Implementation of the LandTrendr algorithm on Google Earth Engine. *Remote Sens.* 10, 1–10. <https://doi.org/10.3390/rs10050691>.
- Kim, P.S., Jacob, D.J., Mickley, L.J., Kopplitz, S.N., Marlier, M.E., DeFries, R.S., Myers, S.S., Chew, B.N., Mao, Y.H., 2015. Sensitivity of population smoke exposure to fire locations in Equatorial Asia. *Atmos. Environ.* 102, 11–17. <https://doi.org/10.1016/j.atmosenv.2014.09.045>.
- Kopplitz, S.N., Mickley, L.J., Marlier, M.E., Buonocore, J.J., Kim, P.S., Liu, T., Sulprizio, M.P., DeFries, R.S., Jacob, D.J., Schwartz, J., Pongpiri, M., Myers, S.S., 2016. Public health impacts of the severe haze in Equatorial Asia in September–October 2015: demonstration of a new framework for informing fire management strategies to reduce downwind smoke exposure. *Environ. Res. Lett.* 11, 094023. <https://doi.org/10.1088/1748-9326/11/9/094023>.
- Kopplitz, S.N., Mickley, L.J., Jacob, D.J., Marlier, M.E., DeFries, R.S., Gaveau, D.L.A., Locatelli, B., Reid, J.S., Xian, P., Myers, S.S., 2018a. Role of the Madden-Julian Oscillation in the transport of smoke from Sumatra to the Malay Peninsula during severe non-El Niño haze events. *J. Geophys. Res. Atmos.* 123, 6282–6294. <https://doi.org/10.1029/2018JD028533>.
- Kopplitz, S.N., Nolte, C.G., Pouliot, G.A., Vukovich, J.M., Beidler, J., 2018b. Influence of uncertainties in burned area estimates on modeled wildland fire PM_{2.5} and ozone pollution in the contiguous U.S. *Atmos. Environ.* 191, 328–339. <https://doi.org/10.1016/j.atmosenv.2018.08.020>.
- Li, F., Martin, M.V., Andreae, M.O., Arneth, A., Hantson, S., Kaiser, J.W., Lasslop, G., Yue, C., Bachelet, D., Forrest, M., Kluzek, E., Liu, X., Mangeon, S., Melton, J.R., Ward, D.S., Darnenov, A.S., Hickler, T., Ichoku, C., Magi, B.I., Sitch, S., van der Werf, G.R., Wiedinmyer, C., Rabin, S., 2019. Historical (1700–2012) global multi-model estimates of the fire emissions from the Fire Modeling Intercomparison Project (FireMIP). *Atmos. Chem. Phys.* 19, 12545–12567. <https://doi.org/10.5194/acp-2019-37>.
- Liu, T., Marlier, M.E., Karambelas, A., Jain, M., Singh, S., Singh, M.K., Gautam, R., DeFries, R.S., 2019. Missing emissions from post-monsoon agricultural fires in northwestern India: regional limitations of MODIS burned area and active fire products. *Environ. Res. Commun.* 1, 011007. <https://doi.org/10.1088/2515-7620/ab056c>.
- Maasakkers, J.D., Jacob, D.J., Sulprizio, M.P., Turner, A.J., Weitz, M., Wirth, T., Hight, C., DeFigueiredo, M., Desai, M., Schmeltz, R., Hockstad, L., Bloom, A.A., Bowman, K.W., Jeong, S., Fischer, M.L., 2016. Gridded National Inventory of U.S. Methane Emissions. *Environ. Sci. Technol.* 50, 13123–13133. <https://doi.org/10.1021/acs.est.6b02878>.
- Marlier, M.E., DeFries, R.S., Kim, P.S., Kopplitz, S.N., Jacob, D.J., Mickley, L.J., Myers, S.S., 2015. Fire emissions and regional air quality impacts from fires in oil palm, timber, and logging concessions in Indonesia. *Environ. Res. Lett.* 10, 085005. <https://doi.org/10.1088/1748-9326/10/8/085005>.
- Marlier, M.E., Liu, T., Yu, K., Buonocore, J.J., Kopplitz, S.N., DeFries, R.S., Mickley, L.J., Jacob, D.J., Schwartz, J., Wardhana, B.S., Myers, S.S., 2019. Fires, smoke exposure, and public health: an integrative framework to maximize health benefits from Peatland restoration. *GeoHealth* 3, 178–189. <https://doi.org/10.1029/2019GH000191>.
- Olson, D.M., Dinerstein, E., Wikramanayake, E.D., Burgess, N.D., Powell, G.V.N., Underwood, E.C., D'Amico, J.A., Itoua, I., Strand, H.E., Morrison, J.C., Loucks, C.J., Allnutt, T.F., Ricketts, T.H., Kura, Y., Lamoreux, J.F., Wettengel, W.W., Hedao, P., Kassem, K.R., 2001. Terrestrial ecoregions of the world: a new map of life on earth. *Bioscience* 51, 933. [https://doi.org/10.1641/0006-3568\(2001\)051\[0933:TEOTWA\]2.0.CO;2](https://doi.org/10.1641/0006-3568(2001)051[0933:TEOTWA]2.0.CO;2).
- Page, S., Hoscilo, A., Langner, A., Tansey, K., Siegert, F., Limin, S., Rieley, J., 2009. Tropical peatland fires in Southeast Asia. In: *Tropical Fire Ecology: Climate Change, Land Use, and Ecosystem Dynamics*. Springer Berlin Heidelberg, Berlin, Heidelberg, pp. 263–287. https://doi.org/10.1007/978-3-540-77381-8_9.
- Prentice, I.C., Kelley, D.I., Foster, P.N., Friedlingstein, P., Harrison, S.P., Bartlein, P.J., 2011. Modeling fire and the terrestrial carbon balance. *Glob. Biogeochem. Cycles* 25, GB3005. <https://doi.org/10.1029/2010GB003906>.
- Randerson, J.T., Chen, Y., van der Werf, G.R., Rogers, B.M., Morton, D.C., 2012. Global burned area and biomass burning emissions from small fires. *J. Geophys. Res.* Biogeosci. 117, G04012. <https://doi.org/10.1029/2012JG002128>.
- Rein, G., Cleaver, N., Ashton, C., Pironi, P., Torero, J.L., 2008. The severity of smouldering peat fires and damage to the forest soil. *Catena* 74, 304–309. <https://doi.org/10.1016/j.catena.2008.05.008>.
- Rogers, B.M., Soja, A.J., Goulden, M.L., Randerson, J.T., 2015. Influence of tree species on continental differences in boreal fires and climate feedbacks. *Nat. Geosci.* 8, 228–234. <https://doi.org/10.1038/ngeo2352>.
- Roteta, E., Bastarrica, A., Padilla, M., Storm, T., Chuvieco, E., 2019. Development of a Sentinel-2 burned area algorithm: generation of a small fire database for sub-Saharan Africa. *Remote Sens. Environ.* 222, 1–17. <https://doi.org/10.1016/j.rse.2018.12.011>.
- Schroeder, W., Giglio, L., 2017. Visible Infrared Imaging Radiometer Suite (VIIRS) 375 m & 750 m Active Fire Detection Data Sets Based on NASA VIIRS Land Science Investigator Processing System (SIPS) Reprocessed Data - Version 1.
- Shi, Y., Matsunaga, T., Saito, M., Yamaguchi, Y., Chen, X., 2015. Comparison of global inventories of CO₂ emissions from biomass burning during 2002–2011 derived from multiple satellite products. *Environ. Pollut.* 206, 479–487. <https://doi.org/10.1016/j.envpol.2015.08.009>.
- Stockwell, C.E., Jayarathne, T., Cochrane, M.A., Ryan, K.C., Putra, E.L., Saharjo, B.H., Nurhayati, A.D., Albar, I., Blake, D.R., Simpson, L.J., Stone, E.A., Yokelson, R.J., 2016. Field measurements of trace gases and aerosols emitted by peat fires in Central Kalimantan, Indonesia, during the 2015 El Niño. *Atmos. Chem. Phys.* 16, 11711–11732. <https://doi.org/10.5194/acp-16-11711-2016>.
- Sulla-Menashe, D., Gray, J.M., Abercrombie, S.P., Friedl, M.A., 2019. Hierarchical mapping of annual global land cover 2001 to present: the MODIS Collection 6 Land Cover product. *Remote Sens. Environ.* 222, 183–194. <https://doi.org/10.1016/j.rse.2018.12.013>.
- Tosca, M.G., Randerson, J.T., Zender, C.S., 2013. Global impact of smoke aerosols from landscape fires on climate and the Hadley circulation. *Atmos. Chem. Phys.* 13, 5227–5241. <https://doi.org/10.5194/acp-13-5227-2013>.
- van der Werf, G.R., Dempewolf, J., Trigg, S.N., Randerson, J.T., Kasibhatla, P.S., Giglio, L., Murdiyasar, D., Peters, W., Morton, D.C., Collatz, G.J., Dolman, A.J., DeFries, R.S., 2008. Climate regulation of fire emissions and deforestation in equatorial Asia. *Proc. Natl. Acad. Sci.* 105, 20350–20355. <https://doi.org/10.1073/pnas.0803375105>.
- van der Werf, G.R., Randerson, J.T., Giglio, L., Collatz, G.J., Mu, M., Kasibhatla, P.S., Morton, D.C., DeFries, R.S., Jin, Y., Van Leeuwen, T.T., 2010. Global fire emissions and the contribution of deforestation, savanna, forest, agricultural, and peat fires (1997–2009). *Atmos. Chem. Phys.* 10, 11707–11735. <https://doi.org/10.5194/acp-10-11707-2010>.
- van der Werf, G.R., Randerson, J.T., Giglio, L., van Leeuwen, T.T., Chen, Y., Rogers, B.M., Mu, M., van Marle, M.J.E., Morton, D.C., Collatz, G.J., Yokelson, R.J., Kasibhatla, P.S., 2017. Global fire emissions estimates during 1997–2016. *Earth Syst. Sci. Data* 9, 697–720. <https://doi.org/10.5194/essd-9-697-2017>.
- Weiss, D.J., Nelson, A., Gibson, H.S., Temperley, W., Peedell, S., Lieber, A., Hancher, M., Poyart, E., Belchior, S., Fullman, N., Mappin, B., Dalrymple, U., Rozier, J., Lucas, T.C.D., Howes, R.E., Tusting, L.S., Kang, S.Y., Cameron, E., Bisanzio, D., Battle, K.E., Bhatt, S., Gething, P.W., 2018. A global map of travel time to cities to assess inequalities in accessibility in 2015. *Nature* 553, 333–336. <https://doi.org/10.1038/nature25181>.
- Wiedinmyer, C., Akagi, S.K., Yokelson, R.J., Emmons, L.K., Orlando, J.J., Soja, A.J., 2011. The Fire Inventory from NCAR (FINN): a high resolution global model to estimate the emissions from open burning. *Geosci. Model Dev.* 4, 625–641. <https://doi.org/10.5194/gmd-4-625-2011>.
- Wilson, A.M., Jetz, W., 2016. Remotely sensed high-resolution global cloud dynamics for predicting ecosystem and biodiversity distributions. *PLoS Biol.* 14, 1–20. <https://doi.org/10.1371/journal.pbio.1002415>.
- Wooster, M.J., Roberts, G., Perry, G.L.W., Kaufman, Y.J., 2005. Retrieval of biomass combustion rates and totals from fire radiative power observations: FRP derivation and calibration relationships between biomass consumption and fire radiative energy release. *J. Geophys. Res. Atmos.* 110, D24311. <https://doi.org/10.1029/2005JD006318>.
- Xiang, H., Liu, J., Cao, C., Xu, M., 2013. Algorithms for Moderate Resolution Imaging Spectroradiometer cloud-free image compositing. *J. Appl. Remote. Sens.* 7, 073486. <https://doi.org/10.1117/1.JRS.7.073486>.
- Xu, J., Morris, P.J., Liu, J., Holden, J., 2018. PEATMAP: refining estimates of global peatland distribution based on a meta-analysis. *Catena* 160, 134–140. <https://doi.org/10.1016/j.catena.2017.09.010>.
- Yi, Y., Kimball, J.S., Reichle, R.H., 2014. Spring hydrology determines summer net carbon uptake in northern ecosystems. *Environ. Res. Lett.* 9, 064003. <https://doi.org/10.1088/1748-9326/9/6/064003>.
- Zhang, F., Wang, J., Ichoku, C., Hyer, E.J., Yang, Z., Ge, C., Su, S., Zhang, X., Kondragunta, S., Kaiser, J.W., Wiedinmyer, C., da Silva, A., 2014. Sensitivity of mesoscale modeling of smoke direct radiative effect to the emission inventory: a case study in northern sub-Saharan African region. *Environ. Res. Lett.* 9, 075002. <https://doi.org/10.1088/1748-9326/9/7/075002>.
- Zhang, T., Wooster, M.J., de Jong, M.C., Xu, W., 2018. How well does the “small fire boost” methodology used within the GFED4.1s fire emissions database represent the timing, location and magnitude of agricultural burning? *Remote Sens.* 10, 823. <https://doi.org/10.3390/rs10060823>.